

**This is a self-archived version of an original article. This version may differ from the original in pagination and typographic details.**

**Author(s):** Kronholm, Risto; Kalvas, Taneli; Koivisto, Hannu; Laulainen, Janne; Marttinen, Miha; Sakildien, Muneer; Tarvainen, Olli

**Title:** Spectroscopic study of ion temperature in minimum-B ECRIS plasma

**Year:** 2019

**Version:** Accepted version (Final draft)

**Copyright:** © 2019 IOP Publishing Ltd.

**Rights:** In Copyright

**Rights url:** <http://rightsstatements.org/page/InC/1.0/?language=en>

**Please cite the original version:**

Kronholm, R., Kalvas, T., Koivisto, H., Laulainen, J., Marttinen, M., Sakildien, M., & Tarvainen, O. (2019). Spectroscopic study of ion temperature in minimum-B ECRIS plasma. *Plasma Sources Science and Technology*, 28(7), 075006. <https://doi.org/10.1088/1361-6595/ab27a1>

ACCEPTED MANUSCRIPT

## Spectroscopic study of ion temperature in minimum-B ECRIS plasma

To cite this article before publication: Risto Kronholm *et al* 2019 *Plasma Sources Sci. Technol.* in press <https://doi.org/10.1088/1361-6595/ab27a1>

### Manuscript version: Accepted Manuscript

Accepted Manuscript is “the version of the article accepted for publication including all changes made as a result of the peer review process, and which may also include the addition to the article by IOP Publishing of a header, an article ID, a cover sheet and/or an ‘Accepted Manuscript’ watermark, but excluding any other editing, typesetting or other changes made by IOP Publishing and/or its licensors”

This Accepted Manuscript is © 2019 IOP Publishing Ltd.

During the embargo period (the 12 month period from the publication of the Version of Record of this article), the Accepted Manuscript is fully protected by copyright and cannot be reused or reposted elsewhere.

As the Version of Record of this article is going to be / has been published on a subscription basis, this Accepted Manuscript is available for reuse under a CC BY-NC-ND 3.0 licence after the 12 month embargo period.

After the embargo period, everyone is permitted to use copy and redistribute this article for non-commercial purposes only, provided that they adhere to all the terms of the licence <https://creativecommons.org/licenses/by-nc-nd/3.0>

Although reasonable endeavours have been taken to obtain all necessary permissions from third parties to include their copyrighted content within this article, their full citation and copyright line may not be present in this Accepted Manuscript version. Before using any content from this article, please refer to the Version of Record on IOPscience once published for full citation and copyright details, as permissions will likely be required. All third party content is fully copyright protected, unless specifically stated otherwise in the figure caption in the Version of Record.

View the [article online](#) for updates and enhancements.

# Spectroscopic study of ion temperature in minimum-B ECRIS plasma

R Kronholm<sup>1</sup>, T Kalvas<sup>1</sup>, H Koivisto<sup>1</sup>, J Laulainen<sup>1</sup>, M Marttinen<sup>1</sup>, M Sakildien<sup>1,2</sup>, O Tarvainen<sup>1,3</sup>

<sup>1</sup> Department of Physics, University of Jyväskylä, Finland

<sup>2</sup> Accelerator Department, iThemba LABS (Laboratory for Accelerator Based Sciences), PO Box 722, Somerset West 7192, South Africa

<sup>3</sup> UK Research and Innovation, STFC Rutherford Appleton Laboratory, Chilton, OX11 0QX, United Kingdom

E-mail: risto.j.kronholm@jyu.fi

## Abstract.

Experimentally determined ion temperatures of different charge states and elements in minimum-B confined electron cyclotron resonance ion source (ECRIS) plasma are reported. It is demonstrated with optical emission spectroscopy, complemented by the energy spread measurements of the extracted ion beams, that the ion temperature in the JYFL 14 GHz ECRIS is 5–28 eV depending on the plasma species and charge state. The reported ion temperatures are an order of magnitude higher than previously deduced from indirect diagnostics and used in simulations, but agree with those reported for a quadrupole mirror fusion experiment. The diagnostics setup and data interpretation are discussed in detail to demonstrate adequate understanding of the line broadening mechanisms and instrumental effects, which justifies the use of the measured Doppler broadening of the emission lines to derive the corresponding ion temperature. The ion temperatures of the high charge state plasma of the minimum-B ECRIS are compared to those measured from low temperature singly charged microwave and arc discharge plasmas to exclude systematic errors. The ion temperatures in the minimum-B ECRIS plasmas are shown to increase with the charge state and injected microwave power whereas two-frequency heating and plasma instabilities have only a minor effect on them. Possible mechanisms causing the higher-than-expected ion temperatures are hypothesized and assessed based on the reported experimental data. Finally, the implications of the results are discussed, demonstrating the need for further experiments especially with charge breeder ECR ion sources, and experimental data on ion confinement times.

## 1. Introduction

Minimum-B Electron Cyclotron Resonance Ion Sources (ECRIS) are used for the production of highly charged heavy ion beams. In the ECR ion source plasma free electrons are heated as a result of energy transfer from microwave electric field to the electrons in relativistic electron cyclotron resonance at the magnetic field isosurface where  $\omega_{ce} = \omega_{RF}$  i.e. when the electron gyrofrequency in the static magnetic field of the ion source equals the frequency of the injected microwave radiation. The resulting electron energy distribution function (EEDF) is non-Maxwellian and is generally treated as three different populations; cold, warm and hot electrons with energies of 10–100 eV, 0.1–10 keV and 10–100 keV, respectively [1]. In order to produce highly charged ions (HCI) it is necessary for the ions to undergo multiple ionizing collisions with electrons. Thus, a long ion confinement time and a sufficient electron density are required for HCI production. The ionization potential increases with the charge state of the ion, which implies that the electron (average) energy needs to be sufficiently high, up to 1 keV order of magnitude, to reach the desired charge states with mass-to-charge  $M/Q$ -ratio of 3–5 (in atomic mass unit / charge state), used often for nuclear physics experiments. Contrary to the ionization process, charge exchange between the highly charged ion and neutral atom can reduce the charge state. Therefore, low neutral gas pressure is important for HCI production. Unlike the magnetized electrons, ions are considered to be electrostatically confined as their high collisionality prevents magnetic confinement, i.e. the ion-ion collision frequency of high charge state ions exceeds their gyrofrequency. In a widely accepted model, suggested by Pastukhov [2], the ions are electrostatically confined in a potential dip of the plasma potential profile, formed as a consequence of the well-confined hot electron population accumulating to the plasma core of the minimum-B ECRIS where  $B < B_{ECR}$  [3, 4, 5]. In this model the ion confinement (of charge  $q$ ) is strongly affected by the depth of the potential dip  $\Delta\phi$  and the ion temperature  $T_i$  as the confinement time  $\tau_{conf} \propto e^{q\Delta\phi/kT_i}$  [6, 7].

The ion energy distribution function (IEDF) of minimum-B ECRISs and the corresponding ion temperature, have not been thoroughly studied mainly due to the complexity of the required measurement setup. Studying the ion temperature is challenging as invasive diagnostic methods inherently affect the plasma properties. A suitable non-invasive and direct diagnostic method is optical emission spectroscopy (OES). Using OES to characterize ECRIS plasmas and to measure the ion temperature through Doppler broadening requires a setup with a good signal-to-noise ratio (SNR) as the emission lines of high charge state ions are often weak in their intensities. Furthermore, a high resolution is required to resolve the Doppler broadening from instrumental effects and other broadening mechanisms. Studying the ion temperature of ECRIS plasmas is relevant for several reasons. The ion temperature affects their confinement through the ion collisionality (magnetic confinement) and escape rate from the potential dip (electrostatic confinement). Thus, experimentally determined ion temperatures can be used for assessing the validity of different confinement models

### *Spectroscopic study of ion temperature in minimum-B ECRIS plasma*

including those based on the potential dip and ambipolar diffusion [6, 8]. Furthermore, several numerical ECRIS plasma simulations use the ion temperature as an input parameter [9] or utilize assumptions that imply low ion temperature for all charge states [10]. The ion temperature also affects the ion beam quality and transport as it contributes to the emittance of the extracted ion beam [11] whereas in charge breeder ECR ion sources the  $1+$  ion capture depends strongly on the ion temperature [12].

Direct ion temperature measurements on ECRIS plasmas hardly exist. Based on extracted currents of high charge state ions and the power balance of the ECRIS plasma Melin et al. [7] argue that the ions are cold compared even to the cold electron population with their temperature ranging from 0.5 eV to 2.0 eV and being the same for all charge states due to high ion-ion collision frequency. Effective ion temperatures have been measured in Ref. [13] indirectly from the extracted beam using a retarding field analyzer, reporting temperatures of 10–30 eV depending on the ion species and increasing with the charge state. In Ref. [14] the ion temperature of the Constance-B quadrupole mirror confinement device, which is essentially similar to a minimum-B ECRIS, has been measured with OES. A high resolution spectrometer was used to measure the Doppler broadening of oxygen emission lines in that work. Approximately 20 eV ion temperatures were obtained without Ion Cyclotron Resonance Heating (ICRH) and 30–500 eV with the ICRH applied. It was also reported that the temperature of ions escaping from the Constance-B device is substantially higher than those probed by OES, the deviation increasing linearly with the (oxygen) charge state [14, 15].

In this study, a high resolution spectrometer [17] was connected to the JYFL† 14 GHz minimum-B ECRIS [18] and the Doppler broadening of a number of emission lines of neutral atoms and ions (He, N, Ne and Ar) was measured in continuous operation mode of the ion source. The results indicate that the temperatures of neutral atoms are in the range of 1–6 eV whereas the temperatures of the ions are in the range of 10–30 eV, depending on the ion charge state. These temperatures are higher than is generally assumed [7] and therefore used in numerical simulations. Hence, this study can be expected to motivate further experiments and to have a high impact on theoretical studies and simulations of ECRIS plasmas. In subsequent sections different optical emission line broadening mechanisms will be discussed to demonstrate that they can be excluded in our case and the characteristics of Doppler broadening can be identified from the observed emission lines. The ion temperatures are determined from the line broadening of different elements and charge states, and compared to the effective ion temperatures measured earlier with the retarding field analyzer. Finally, the implications of the ion temperature on the confinement of high charge state ions is discussed together with possible ion heating mechanisms.

† JYFL stands for Jyväskylän Yliopiston Fysiikan Laitos i.e. Finnish for University of Jyväskylä, Department of Physics

## 2. Line broadening mechanisms and profiles

Using optical emission line broadening as a diagnostic method requires identifying and resolving the effects of different broadening mechanisms on the line width. Fortunately each broadening mechanism has a specific wavelength dependence as explained hereafter. Furthermore, the magnitude of the broadening effect depends on the type of the transition (upper and lower states), which can be used to identify the broadening mechanism responsible for the experimental observation. The main optical emission line broadening mechanisms are:

- Doppler broadening
- Natural broadening
- Collisional/Pressure broadening
- Stark broadening
- Resonance broadening
- Van der Waals broadening
- Zeeman broadening
- Broadening due to measurement geometry and plasma drifts
- Instrumental broadening

In the above list, the last two are caused by the measurement setup and geometry whereas the rest are due to fundamental physics as described below.

### 2.1. Doppler broadening

In plasma individual atoms and ions have a velocity component  $v$  towards or away from the observer, which in the case discussed hereafter is the optical output from the ECRIS plasma chamber. When the atom or ion emits a photon with a frequency of  $f_0$ , the observer detects the radiation at the frequency

$$f = f_0 \left( 1 \pm \frac{v}{c} \right), \quad (1)$$

where the  $+$  and  $-$  signs correspond to an approaching and receding source, respectively. The distribution of individual Doppler shifts of an ensemble of sources can be derived from the corresponding (one-dimensional) distribution of velocities along the line of sight. For convenience it is assumed that the velocity distribution is Maxwellian i.e.

$$n(v) dv = \sqrt{\frac{m_i}{2\pi k_B T}} \exp\left(\frac{-m_i v^2}{2k_B T}\right) dv, \quad (2)$$

where  $n(v)$  is the number of particles within the velocity interval  $v + dv$ ,  $m_i$  is the ion (or neutral atom) mass and  $k_b T$  is their temperature. Substituting the velocity derived

## Spectroscopic study of ion temperature in minimum- $B$ ECRIS plasma

from Eq. 1, we obtain the intensity distribution function of frequencies around the center frequency  $f_0$

$$I(f) = I_{f0} \exp \left( -\frac{m_i c^2 (f_0 - f)^2}{2k_B T f_0^2} \right). \quad (3)$$

This distribution has a Gaussian profile and is called the Doppler profile of an emission line. The full width at half maximum (FWHM) of the line broadening is given by

$$\frac{\Delta f}{f_0} = \frac{\Delta \lambda}{\lambda_0} = 2\sqrt{2 \ln 2} \frac{k_B T}{m_i c^2}, \quad (4)$$

where  $\sqrt{\frac{k_B T}{m_i c^2}}$  is the standard deviation of the (normal) distribution of frequencies and corresponding wavelengths. Thus, for Doppler broadening of a given ion species  $\Delta \lambda \propto \lambda_0$ . It is worth noting also that  $\Delta \lambda \propto 1/\sqrt{m_i}$  resulting to an isotopic effect of a given emission line. Both of these dependencies can be used for resolving the Doppler broadening (temperature dependent) from other line broadening mechanisms as discussed in section 4. Measuring the Doppler broadening of the emission lines in ECRIS plasmas requires the resolution of the spectrometer to be on the order of picometers as, for example, the thermal Doppler FWHM of 10 eV Ar<sup>13+</sup> (441.2556 nm) is approximately 17 pm.

In ECRIS plasmas ions are moving in a complex electromagnetic field and can therefore, depending on the ratio of ion collision and gyrofrequencies, be subjected to bulk motion such as rotation or local plasma drifts, e.g. the  $E \times B$ -drift and gradient-curvature-drift. In addition to Doppler broadening caused by thermal motion, such bulk movement can result to Doppler shift and subsequent broadening of emission lines, which is utilized e.g. for measuring the speed of plasma rotation in centrifugal confinement machines and tokamaks. The observed broadening of the emission lines could therefore depend on the measurement geometry, which needs to be excluded when assessing the ion temperature derived from OES by comparing the Doppler broadening profiles of the emission lines measured from different viewing (solid) angles as reported in section 4.

### 2.2. Natural broadening

Natural broadening of emission lines follows from the Heisenberg uncertainty principle  $\Delta E \Delta t > \hbar/2$ . The quantum mechanical uncertainty of the energy levels with finite intrinsic lifetimes generates broadening of the corresponding emission lines. The emission line width of a decay with an upper state lifetime of 10 ns, typical for the transitions studied hereafter and listed in Tables A1–A4 of the Appendix is on the order of  $10^{-7}$  eV [19], which is small in comparison to the Doppler broadening corresponding to 1 eV thermal spread and cannot be resolved with most high-resolution spectrometers. This broadening mechanism gives rise to a Lorentzian emission line profile.

## Spectroscopic study of ion temperature in minimum-B ECRIS plasma

6

### 2.3. Pressure broadening

The pressure broadening can be considered as a superposition of multiple different broadening mechanisms. The broadening is caused by the electromagnetic interaction between the emitter and its neighbouring particles. The energy exchange between the interacting particles in collisions of atoms and ions can reduce the effective lifetime of an electronic state and lead to broadening of the emission lines. The line broadening  $\Delta f$  of a transition emitting a photon at the wavelength  $\lambda$  is given by

$$\Delta f = \frac{\Delta \lambda}{\lambda^2} c = \frac{1}{2\pi\tau}, \quad (5)$$

where  $\tau$  is the mean time between collisions. Thus, it follows that the magnitude of collisional broadening due to the presence of an electric force depends on the emission wavelength as  $\Delta \lambda \propto \lambda^2$  for a given charge state ion (constant  $\tau$ ). Contrary to Doppler broadening, pressure broadening leads to Lorentzian emission line profile, which can be used for identifying the broadening mechanism from experimentally determined emission lines. The contribution of the collisional broadening on the observed emission line profile depends strongly on the gas pressure and charged particle density due to the effect of the collision time i.e.  $\Delta \lambda \propto \tau^{-1} \propto n$ , where  $n$  is the particle density. In ECRIS plasmas where the ion-ion collision frequency of high charge state ions (dominating collision process) is on the order of  $10^8$  Hz as a maximum [7], the intrinsic collisional broadening of e.g. the 488 nm emission line of  $\text{Ar}^{1+}$  (studied later) can be estimated to be on the order of 0.01 pm, which is well below the instrumental broadening of the spectrometer described later.

The exact mechanisms contributing to the pressure broadening can be classified by the nature of the perturbing force [20]. For example, collisions between identical particles can lead to so-called resonance broadening, which is limited to emission lines corresponding to electrical dipole transitions to the ground state [21]. In addition to intrinsic fields due to surrounding charged particles, ions in ECRIS plasma are under the influence of external electric fields e.g. due to sheath potentials and microwave radiation. Atoms and ions with an electric dipole moment experience a splitting of their energy levels under the influence of an electric field. This splitting which can exceed the intrinsic collisional broadening and affect the measured line profile is called the Stark effect. The energy shift  $\Delta \epsilon$  and subsequent line broadening due to the Stark effect is a superposition of linear and quadratic (to the electric field) terms [22]. The linear Stark effect caused by point-like charge, i.e. under the influence of a neighbouring particle, is of the form

$$\Delta \epsilon^{(E_0)} \approx q_e a_0 E_0 S = q_e a_0 S \left( \frac{q}{4\pi\epsilon_0 r_0^2} \right), \quad (6)$$

where  $q_e a_0 E_0 S$  is the atomic dipole moment of the upper energy level of the electronic transition and  $E_0$  is the local electric field [22]. The quadratic Stark effect is of the form

$$\Delta \epsilon^{(E_0)} \approx \frac{q_e^2 a_0^2 S^2}{\hbar \omega_{ij}} E_0^2, \quad (7)$$



## Spectroscopic study of ion temperature in minimum- $B$ ECRIS plasma

7

where  $\hbar\omega_{ij}$  is the energy difference between the upper and lower states  $i$  and  $j$  [22]. The sensitivity of a spectral line to the Stark effect depends strongly on the specific electronic state of the atom or ion. Thus, a comparison of different emission lines' linewidths of a given emitting particle can be used for assessing the contribution of the Stark effect on the experimentally observed line shape. Experimental results for Stark line widths and shifts can be found from Ref. [23], where the Stark broadenings of  $\text{Ar}^{1+}$  transitions measured in this paper (see Section 4) are listed. Although the discharge conditions in the ECRIS plasma are different, the data in Ref. [23] indicates that Stark broadening would cause a factor of two difference in line broadenings among the specific transitions without a specific dependence on the wavelength whereas the experimentally observed line widths deviate from each other much less, and exhibit a linear dependence on the wavelength as shown later in Fig. 5. Thus, it is concluded that although there are static and time-varying electric fields in ECRIS plasmas, their contribution to observed line broadening is negligible. Finally, van der Waals broadening occurs when the emitting particle (electronically excited atom) is perturbed by a neutral atom via van der Waals dipolar interactions [22, 24]. Such an effect is often negligible in comparison to other broadening mechanisms under discharge conditions typical to ECRIS.

### 2.4. Zeeman broadening

Zeeman effect (broadening) refers to the splitting of spectral lines into several components in the presence of a static magnetic field  $B$  and the corresponding broadening of the detected spectral line. The shift  $\Delta E$  of the atom/ion energy levels depends on the upper and lower states of the transition as

$$\Delta E_B = \vec{\mu} \cdot \vec{B} = -\mu_B g_L m_J B, \quad (8)$$

where  $g_L$  is the Landé g-factor,  $\mu_B$  is the Bohr magneton and  $m_J$  is the projection of the total angular momentum  $J = L + S$  of the quantum state. The corresponding change of the emission wavelength  $\Delta\lambda$  can be written for small change in energy as

$$\Delta\lambda = -\frac{\lambda^2}{hc} \Delta E_B, \quad (9)$$

i.e. the shift (broadening) depends quadratically on the wavelength of the emitted radiation, similar to Stark effect. Zeeman broadenings for helium and argon are reported for example in Ref. [25] in magnetic fields of 0.5–1.1 T relevant for ECRIS plasmas. The observed Zeeman-broadening for the 587 nm and 811 nm emission lines of He and Ar are 7–16 pm and 18–34 pm, respectively. The emission lines observed in this work are predominantly in the range of 400–500 nm for which the Zeeman broadening can be expected to be  $\leq 5$  pm corresponding to emission from the dense core of the ECRIS plasma where  $B \leq 0.5$  T.

## Spectroscopic study of ion temperature in minimum-B ECRIS plasma

8

### 2.5. Instrumental broadening

In addition to emission line broadening caused by fundamental physics, the experimental setup and apparatus result in instrumental broadening of the observed emission lines. In the experimental setup used in this study, the instrumental broadening has a Gaussian profile. Its wavelength dependence can be calculated and verified with a laser (632 nm HeNe + 532 nm diode-pumped frequency-doubled single-mode laser). The instrumental broadening, which in our setup is comparable to the Doppler broadening, and its wavelength dependence are discussed in detail in Section 3.

### 2.6. Voigt profile

As the line broadening is a superposition of multiple mechanisms yielding both, Gaussian and Lorentzian line shapes, a convolution of the two must be used when analyzing the experimental line profiles. The convolution is called a Voigt profile

$$V(x; \sigma, \gamma) = \int_{-\infty}^{\infty} G(x'; \sigma) L(x - x'; \gamma) dx', \quad (10)$$

in which  $x$  is the shift from the line center,  $G(x; \sigma)$  describes the Gaussian profile

$$G(x; \sigma) = \frac{e^{-x^2/2\sigma^2}}{\sqrt{2\pi}\sigma}, \quad (11)$$

where  $\sigma$  is the standard deviation and  $L(x - x'; \gamma)$  the Lorentzian profile

$$L(x; \gamma) = \frac{\gamma}{\pi(x^2 + \gamma^2)}, \quad (12)$$

where  $\gamma$  is the half-width at half-maximum (of the line profile). Deconvolution of the Voigt fit allows the Gaussian and Lorentzian contributions to be separated. Each component of the Voigt line profile is a superposition of different broadening mechanisms. For the purpose of this study the Doppler broadening and the instrumental broadening, both giving rise to a Gaussian line profile, have to be separated to obtain the ion temperature. The Doppler broadening  $\Delta\lambda_D$  can be separated from the instrumental broadening  $\Delta\lambda_I$  with a quadratic deconvolution

$$\Delta\lambda_D^2 = \Delta\lambda_G^2 - \Delta\lambda_I^2. \quad (13)$$

where  $\Delta\lambda_G$  is the Gaussian part of the Voigt deconvolution [26]. Determining the instrumental broadening and excluding the effect of plasma bulk motion (drifts) therefore allows to calculate the ion temperature from the measured line widths.

## 3. Experimental setup

This study has been conducted with the JYFL 14 GHz Electron Cyclotron Resonance Ion Source (ECRIS) [18] and a high resolution spectrometer [17]. The magnetic field of the JYFL 14 GHz ECRIS is a superposition of axial and sextupole magnetic fields generated by two solenoid coils and a NdFeB permanent magnet sextupole array, hence

# *Spectroscopic study of ion temperature in minimum-B ECRIS plasma*

enabling the production of highly charged ions in minimum-B configuration. The plasma is sustained by microwave radiation at the frequency of 14.1 GHz. More detailed information about the JYFL 14 GHz ECRIS, depicted in Fig. 1, can be found in Ref. [18].

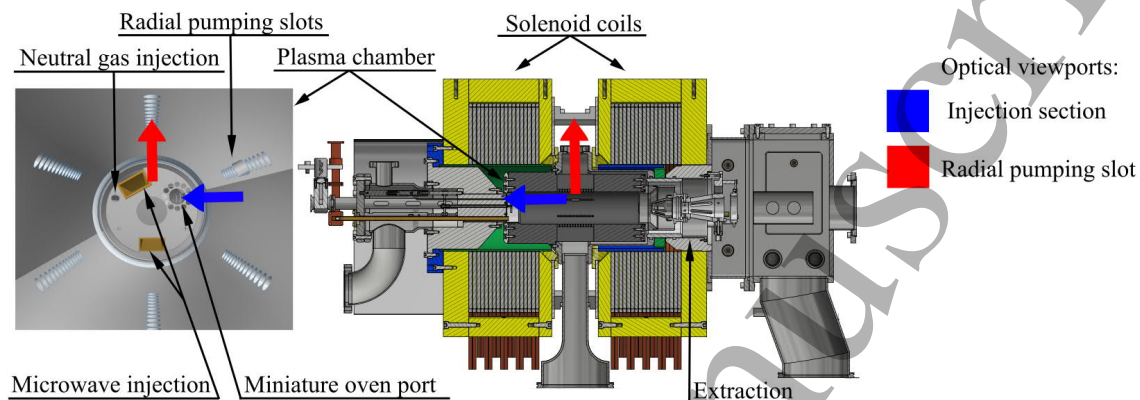


**Figure 1.** The plasma chamber of the JYFL 14 GHz ECRIS viewed towards the injection iron plug from the extraction end (left) and the cross section view of the ion source (right). The radial pumping slot(s) (red) and the miniature oven port (blue) used as optical viewports are indicated by arrows.

The spectrometer consists of three main components; the optical interface, i.e. viewport and coupling system, connected to the ECRIS, high-resolution optical monochromator and photomultiplier tube connected to a phase-locking data acquisition system. The optical emission spectrum of the plasma can be measured from two different viewports having different line-of-sights; from injection utilizing an opening in the iron plug, used regularly for inserting miniature ovens for metal beam production, and from one of the radial pumping slots, both indicated in Fig. 1. The radial line-of-sight, which was used for the majority of the experiments described hereafter, offers a cross sectional view through the plasma sheath and the dense plasma core inside the resonance zone. Since the radial port is situated between the magnetic poles (see the pumping slots in Fig. 1), the emission of the ions escaping the confinement along the magnetic field flux lines intercepting the chamber wall and thus neutralizing is not detected. The line-of-sight from the injection was used to ensure that the geometric effects combined with bulk plasma motion (drift or rotation), do not affect the measured line broadening. The solid angle viewed from the injection also includes the chamber wall. However, as the majority of the upper states of the transitions studied hereafter are not metastable, i.e. their typical lifetimes are on the order of nanoseconds, the contribution of the emission from the plasma chamber wall can be considered negligible also in this case. The effect of the ion dynamics in the collisional pre-sheath on the measured line widths cannot be distinguished from the thermal spread of the ion velocities. The chosen (radial) line-of-sight avoiding the flux intercepting the wall is believed to minimize the pre-sheath effect especially in the case of high charge states found predominantly in the core plasma [9].

# *Spectroscopic study of ion temperature in minimum-B ECRIS plasma* 10

The light emitted by the ECRIS plasma is coupled into an optical fiber which is connected to the monochromator through a chopper providing a reference for the lock-in data acquisition. The monochromator is a Fastie-Ebert type device equipped with a rotating diffraction grating. The focal length of the monochromator is approximately 1 m and the groove density of the diffraction grating is 2200 lines/mm. Two different exit slits, with widths of 100  $\mu\text{m}$  and 10  $\mu\text{m}$ , were used to verify that the ion temperatures reported hereafter are not affected by systematic errors in estimating the instrumental broadening. The benefit of the wider slit is the increased signal level i.e. better signal-to-noise ratio and shorter acquisition time. The instrumental broadening (FWHM) of the setup as a function of the measured wavelength can be calculated from

$$\lambda_{\text{FWHM}}(\text{nm}) = \frac{d\lambda}{dx} \cdot w = \frac{10^6 \cos \beta}{knL} \cdot w, \quad (14)$$

where  $d\lambda/dx$  is the linear dispersion,  $w$  is width of the exit slit,  $k$  is the diffraction order,  $n$  is the groove density in grooves/mm,  $L$  is the exit arm length in mm and  $\beta$  is the angle of diffraction. Three different lasers providing well-known narrow line widths were used for determining the instrumental FWHM in the wavelength range of 450–650 nm. These included a HeNe laser at 632 nm, diode-pumped frequency-doubled single-mode laser at 532 nm and an argon ion laser at 458, 488 and 514 nm. The measured and calculated instrumental FWHMs are presented in Fig. 2 where the solid symbols correspond to HeNe and the diode laser and the open symbols to the argon ion laser. As the measured points match the calculated ones very well, it can be assumed that the calculated values can be used for the deconvolution of the Gaussian fit to the emission lines at those wavelengths that are not directly accessible with the above lasers.

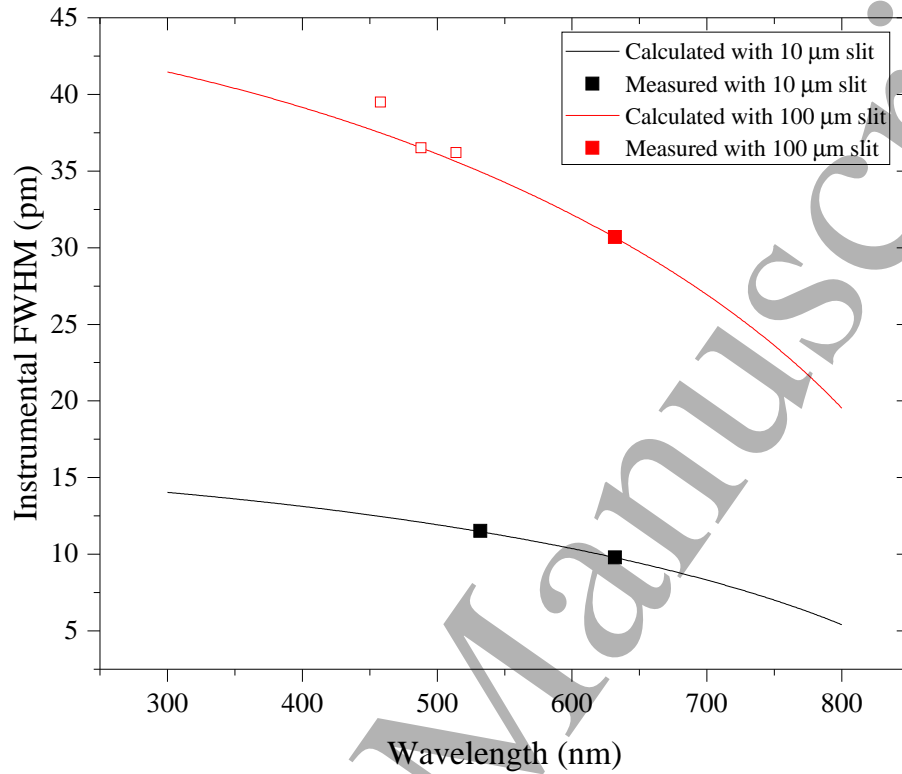


**Figure 2.** Instrumental FWHM of the Fastie-Ebert monochromator as a function of the emission wavelength. The symbols represent the measured data points and the solid lines the theoretical instrumental FWHMs. The solid symbols correspond to HeNe and the diode laser and the open symbols to the argon ion laser. The random error of measured FWHM, determined through consecutive acquisitions of the individual line profiles, is 0.5 pm.

The wavelength separated light signal emanating from the monochromator exit slit is directed into a high sensitivity photomultiplier tube (PMT). The PMT is cooled with Peltier elements to achieve better signal-to-noise ratio and stabilize the output. The output current from the photomultiplier is fed into a current-to-voltage amplifier (Stanford Research Systems SR570). In the amplifier, the signal is amplified with a gain of 1  $\mu\text{A/V}$  and bandpass filtered with a 6 dB/decade high pass filter at 3 kHz and low pass filter at 10 kHz. The signal from the transimpedance amplifier is fed into Stanford Research Systems SR830 lock-in amplifier which is connected to the combined monochromator control and data acquisition system. The data are gathered by averaging 50 (or more) current readings of the PMT at each monochromator grating position scanned across the emission line of interest.

In addition to optical methods the ion temperature of the JYFL 14 GHz ECRIS has been estimated in the past [13] by measuring the energy spread of the M/Q-analyzed ion beams with a retarding field analyzer [27]. The device can be used for measuring

## *Spectroscopic study of ion temperature in minimum-B ECRIS plasma* 12

the plasma potential and effective ion temperature of the extracted beam as the energy of the ions of charge  $q$  is due to the source potential ( $V_s$ ), plasma potential  $V_p$  and ion temperature i.e.  $E = q(V_s + V_p) + kTi$ . The plasma potential and the effective ion temperature can be determined by measuring the beam current as a function of a decelerating voltage ( $V_{dec} = V_s + V_{adj}$ ) applied into the retarding electrode (mesh) of the analyzer. The adjustable voltage supply ( $V_{adj}$ ) for the mesh floats on the high voltage of the ion source ( $V_s$ ), which eliminates the possible measurement error due to the source potential and its possible fluctuation. It is emphasized that both, the spatial distribution of the plasma potential combined with collisional diffusion of the ions to the extraction and the ion temperature cause a distribution of energies to be measured. The plasma potential and effective ion temperature are deduced from the shift (plasma potential) and distribution (effective ion temperature) of the differential IV-curves representing the fraction of ions stopped by the retarding potential barrier at given voltage intervals. The effective ion temperatures of different charge states are deduced by applying a Gaussian fit to the measured differential IV-curves i.e. the effective ion temperature corresponds to the energy spread of the ion beams around the plasma potential, which is equal for all charge states [13].

It is emphasized that probing the effective ion temperature of the extracted beams is fundamentally different from measuring the temperature of the ions confined in the ECRIS plasma. This is because the alleged electrostatic confinement of the ions in the potential dip favours losses of hot ions that have enough energy to overcome the potential barrier and form the extracted beam. Thus, it can be expected that the effective temperature of the beam is higher than the temperature of the ions in the plasma which has indeed been observed with the Constance-B device, where a similar technique was applied to study the energy distribution of ions escaping the confinement [14, 15]. Furthermore, it needs to be emphasized that the connection between the temperature of the electrostatically confined ion population and the effective temperature of the extracted ion beam determined from the energy spread is not unambiguous. It has been shown by Baalrud et al. that ion-ion streaming instabilities, which are present in the plasma-boundary transition region (pre-sheath), can lead to an instability-enhanced collisional friction between the ion species at least in the case of singly charged ions [16]. The friction together with the generalized Bohm criterion determines the flow speed of each ion species as it leaves the plasma effectively slowing down high charge state ions and accelerating low charge states towards a common system sound speed of  $c_s = \sqrt{\frac{\sum_i c_{s,i}^2 n_i}{n_e}}$  instead of their individual, charge-state dependent sound speeds  $c_{s,i} = \sqrt{\frac{qT_e}{M_i}}$  [16]. Such effects presumably could obscure the connection between the plasma ion temperature and ion beam energy spread, which is the reason why we refer to the latter as effective temperature in the absence of experimental data on ion-ion streaming instabilities of minimum-B ECR ion sources in MHz-range of beam current noise. Nevertheless, it can be argued that the two diagnostics methods should yield ion temperatures that are on the same order of magnitude with each other and also

exhibit similar dependencies on the charge state. The results of the optical emission spectroscopy and retarding field analyser are compared in the following section. Such a comparison is carried out to give confidence on the reliability of the measured ion temperatures, which are shown to be significantly higher than those reported in the literature [7] and compare our results to those obtained with the Constance-B machine [14, 15].

**4. Experimental results**

The experiments were started by establishing that the emission lines measured from the ECRIS plasma are Gaussian (rather than Lorentzian) i.e. the observed line width is due to a superposition of instrumental and Doppler broadenings. This was done by measuring emission lines of both low and high charge states, i.e.  $\text{Ar}^{1+}$  and  $\text{Ar}^{13+}$  at 487.986 nm and 441.256 nm, and using different exit slits of the monochromator. The measured emission line profiles are shown in Figs. 3a–c together with the corresponding Voigt fits yielding the Gaussian and Lorentzian components of the line broadening. For  $\text{Ar}^{13+}$  measured with an exit slit of 100  $\mu\text{m}$  the Gaussian and Lorentzian FWHMs are 45.4 pm and 0.8 pm, respectively. For  $\text{Ar}^{+}$  the corresponding numbers are 39.5 pm and  $3 \cdot 10^{-6}$  pm whereas the measurement with a 10  $\mu\text{m}$  exit slits yields the values of 25.5 pm and 2.4 pm for the two components of  $\text{Ar}^{+}$  line broadening.

## Spectroscopic study of ion temperature in minimum-B ECRIS plasma

14

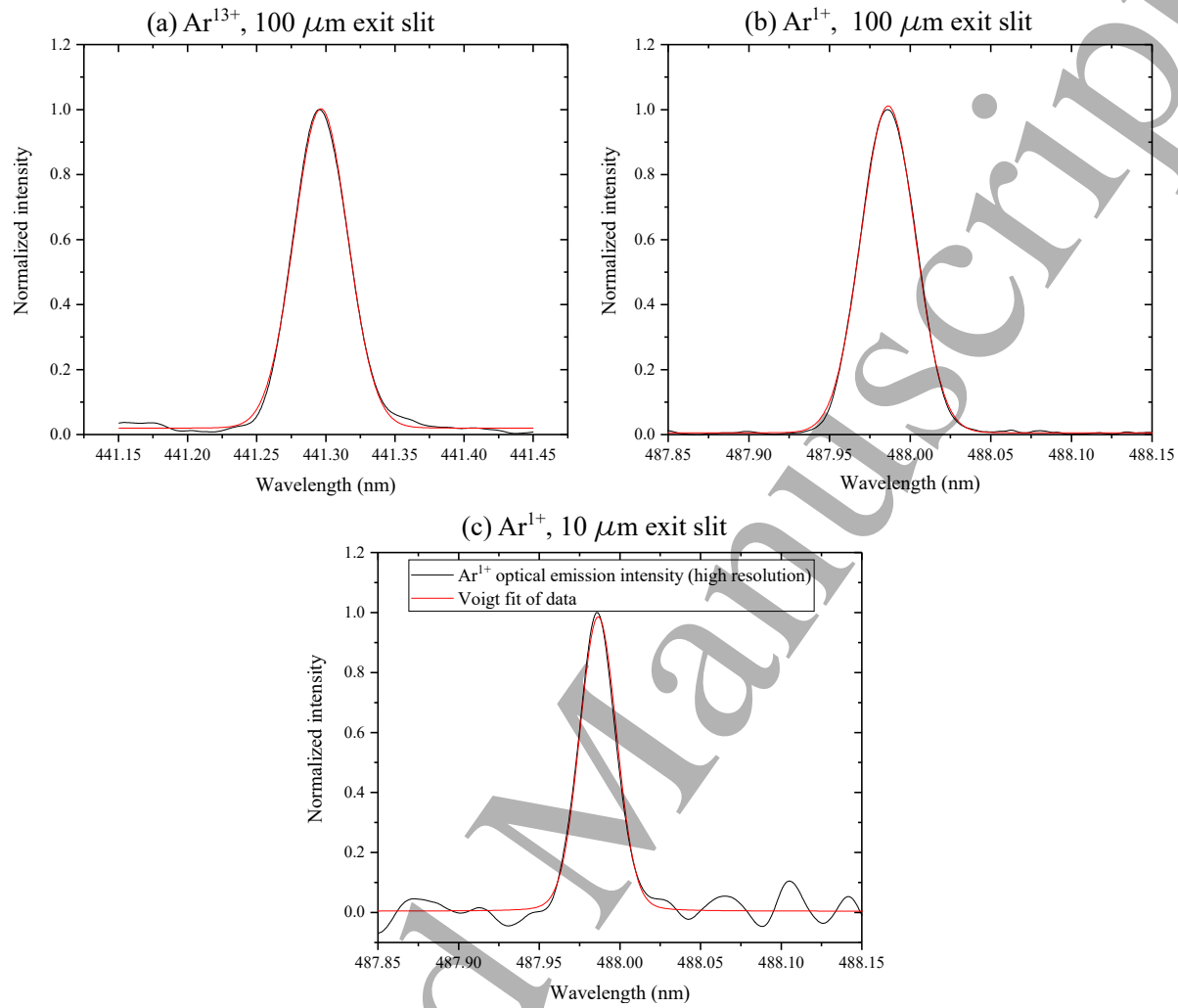


**Figure 3.** Measured optical emission lines of (a) Ar<sup>13+</sup> and (b) Ar<sup>1+</sup> with the 100 μm monochromator exit slit, and (c) Ar<sup>1+</sup> with the 10 μm slit. The black lines represent experimental data while the red ones are the corresponding Voigt fits. The corresponding Voigt fits with the following Gaussian (G) and Lorentzian (L) FWHMs are also shown: (a)  $(45.4 \pm 0.4)$  pm (G) /  $(0.8 \pm 0.5)$  pm (L), (b)  $(39.50 \pm 0.04)$  pm (G) and (c)  $(25.5 \pm 0.7)$  pm (G) /  $(2.4 \pm 0.1)$  pm (L). The Lorentzian FWHM for (b) is smaller than 0.1 pm but cannot be determined accurately for numerical reasons.

Although the examples given in Fig. 3 indicate that the emission lines measured from the ECRIS plasma are indeed Gaussian, it could be argued that the instrumental broadening of the spectrometer prohibits detecting the Lorentzian component of the line broadening. In order to demonstrate that the spectrometer is able to measure Lorentzian line profiles reliably, the 427 nm Ar<sup>1+</sup> emission line measured from the ECRIS plasma was compared to the 362 nm emission line of a neutral Hg measured from a mercury spectral lamp (Osram Hg/100), which is known to produce Lorentzian line profiles with distinguishable “wings” of the emission line due to pressure broadening. The result of the comparison is shown in Fig. 4. The difference of the line shapes is apparent, which establishes that the resolution of the spectrometer is adequate



# *Spectroscopic study of ion temperature in minimum-B ECRIS plasma*

15

for resolving the Gaussian and Lorentzian components of the line broadening. This enables determining the ion temperature through the deconvolution of the broadening mechanisms yielding Gaussian line profiles i.e. subtracting the effect of the wavelength-dependent instrumental broadening (see Fig. 2).

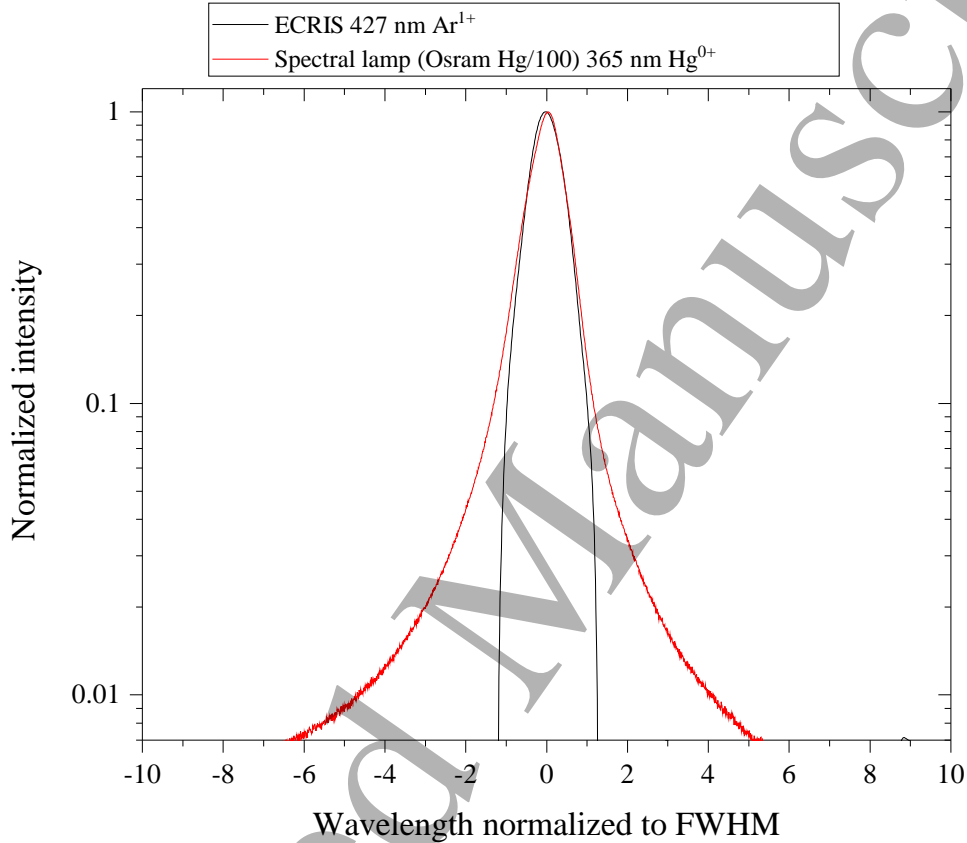


**Figure 4.** An example of the  $\text{Ar}^{1+}$  optical emission line at 427 nm measured from the ECRIS plasma with 10  $\mu\text{m}$  exit slit and the neutral Hg emission line at 362 nm from a spectral lamp (Osram Hg/100). Both emission lines are normalized to their respective intensities and FWHMs. The Gaussian (G) and Lorentzian (L) FWHMs of the Voigt fit are: 1.01 (G) / 0.02 (L) for the  $\text{Ar}^{1+}$  emission line and 0.57 (G) / 0.69 (L) for the neutral Hg line of the spectral lamp. The small asymmetry of the Lorentzian profile is caused by the astigmatism of the monochromator optics.

Before reporting individual ion temperatures or conducting parametric studies, it needs to be established that the deconvoluted line broadening (after the subtraction of the instrumental broadening) is indeed due to the Doppler effect, and that there is no systematic error increasing (or decreasing) the measured ion temperatures. The fact that the line broadening is due to Doppler effect was confirmed with two experiments. First, the line widths of several emission lines of  $\text{Ar}^{+}$  emitted by the ECRIS plasma and covering the wavelength range of 390–620 nm were measured to probe the wavelength dependence of the line broadening. The result is shown in Fig. 5 where the line widths

# Spectroscopic study of ion temperature in minimum-B ECRIS plasma

16

of different emission lines are plotted first as measured and then after subtracting the wavelength dependent instrumental broadening (also shown) through the described deconvolution process. The error bars of the Doppler broadening in Fig. 5 as well as in all consecutive plots of line widths and ion temperatures calculated from Eq. 4 correspond to 95 % confidence interval of the FWHM of the fit to the experimental line profile and take into account the error associated to the instrumental broadening. The fit shown in the figure demonstrates that the wavelength dependence of the line broadening after subtracting the wavelength dependent instrumental effect is of the form  $\Delta\lambda \propto \lambda$ , characteristic to the Doppler effect. The data implies that the contribution of Stark and Zeeman effects on the measured line profiles is negligible and highlights the necessity of determining the wavelength dependence of the instrumental broadening.

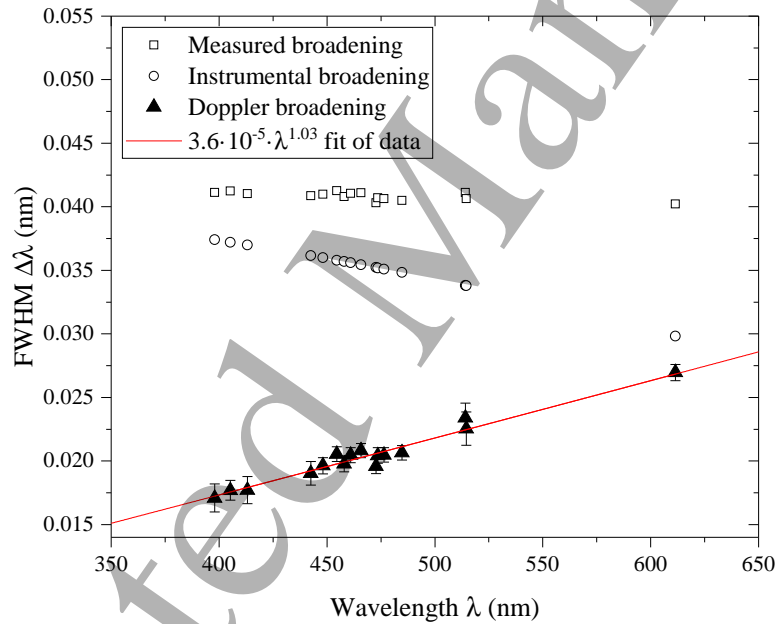


**Figure 5.** The measured, instrumental and Doppler FWHMs of  $\text{Ar}^{1+}$  emission lines as a function of the wavelength. The fit of the Doppler broadening shows that after subtracting the instrumental effect the FWHM is linearly proportional to the wavelength, which is characteristic to Doppler broadening.

The mass-dependence of the line broadening was probed by comparing the line widths of  $^3\text{He}$  and  $^4\text{He}$  isotopes of helium under the same ECR ion source parameters (microwave power, gas pressure and magnetic field) in the range of 400–600 nm. The results are shown in Fig. 6 showing the experimental ratios and the theoretical prediction (blue line) following the  $\Delta\lambda \propto 1/\sqrt{m_i}$ -dependence of the Doppler broadening. It is evident that the experimental data fits well with the expected behaviour thus reasserting the notion that the measured line widths are determined by Doppler broadening and well-understood instrumental broadening, which allows calculating the corresponding

ion temperatures from the experimental line profiles.

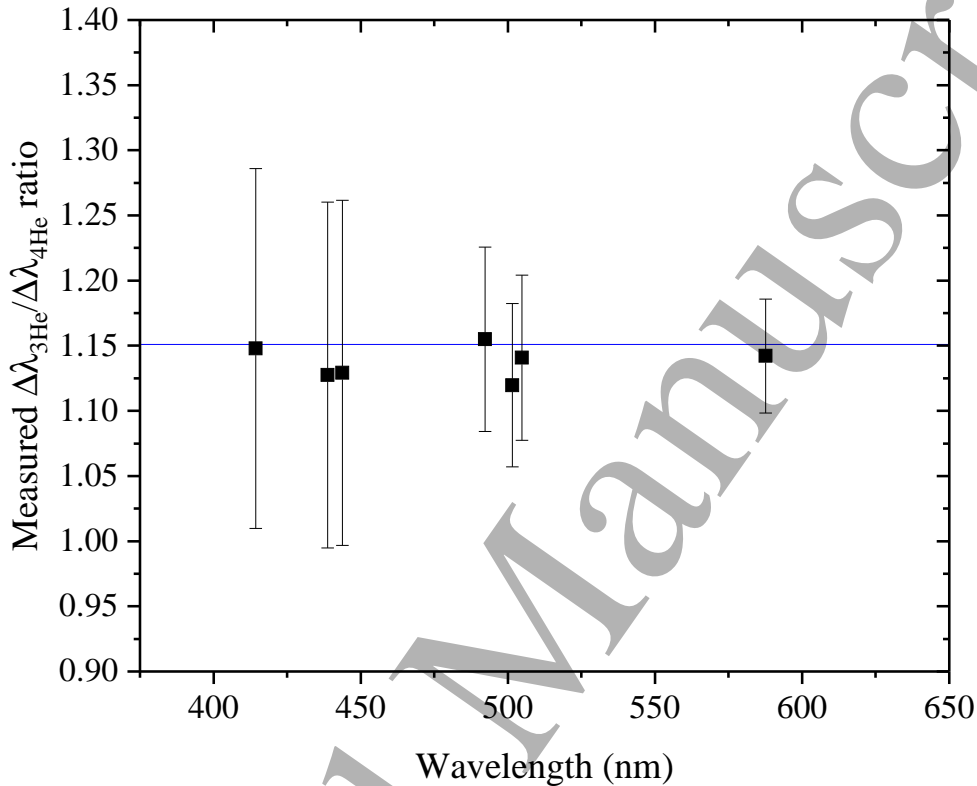


**Figure 6.** The measured ratio of  $^3\text{He}$  and  $^4\text{He}$  Doppler broadening ( $\Delta\lambda_{3\text{He}}/\Delta\lambda_{4\text{He}}$ ). The solid horizontal line indicates the expected  $1/\sqrt{m}$  mass dependence.

The first OES measurement of the ECRIS ion temperature was conducted with argon. Figure 7 shows the  $\text{Ar}^{1+}$  ion temperature determined from multiple optical transitions with two exit slits of the monochromator. All transitions and both slits yield ion temperatures of  $13 \pm 2$  eV, which are significantly higher than those (on the order of  $\sim 1$  eV) estimated previously in the literature through indirect measurements [7] and used in simulation studies [9, 12]. The ion temperature is essentially the same with both slits resulting to different instrumental broadening, which warrants using the wider slit for the subsequent studies. The benefit of the wider slit is that it makes weaker emission lines accessible and improves the signal-to-noise ratio whereas the narrow slit produces smaller error bars.

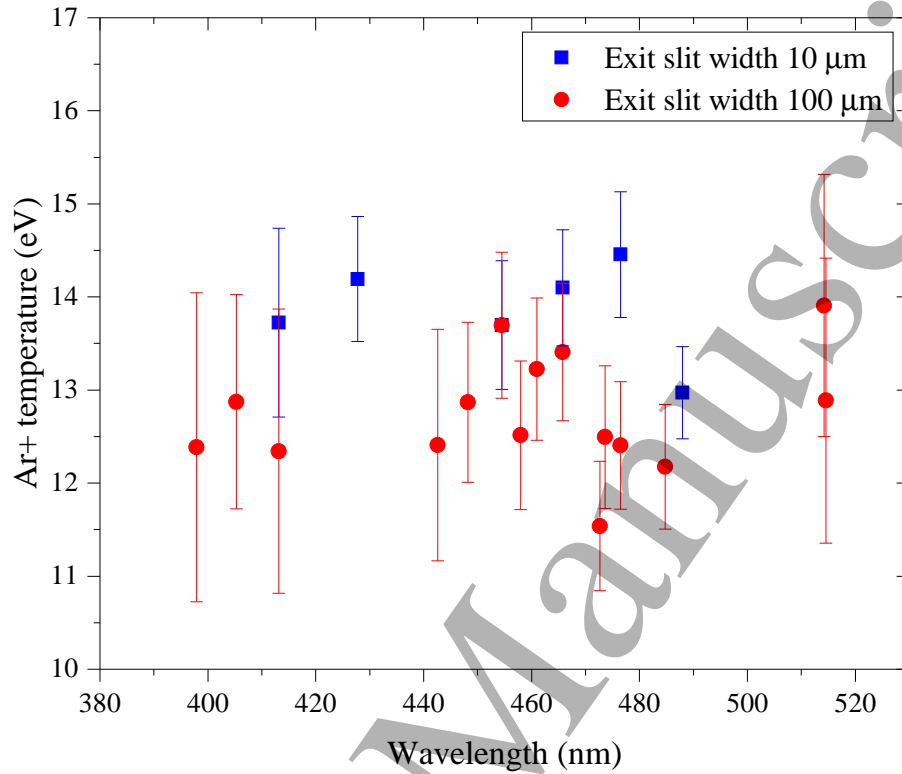


**Figure 7.** The  $\text{Ar}^{1+}$  ion temperatures measured with the high resolution 10  $\mu\text{m}$  and the 100  $\mu\text{m}$  exit slits of the monochromator.

As the measured ion temperature is controversially high, it is necessary to demonstrate that the spectrometer does not suffer from a systematic error. This was done by comparing the ion temperatures of  $\text{Ar}^{1+}$  from different ion source plasmas, namely the JYFL 14 GHz ECRIS, a single-coil 2.45 GHz microwave driven ion source [28] and a filament-driven arc discharge ion source [29] — the latter two expected to have low ion temperatures due to short ion confinement time and high neutral gas pressure. The result of this experiment is shown in Fig. 8. The experiment was conducted by keeping the spectrometer operational (to avoid alignment issues) and routing a long optical fiber to different ion sources across the laboratory. The emission lines of all ion sources were found to be Gaussian. The data demonstrates clearly that the argon ions in the microwave and filament discharges, where the electron confinement is poor and the dominating ion species is singly charged argon, the ion temperature is significantly lower (2–4 eV) than in the high-frequency minimum-B ECRIS producing multicharged ions (11–16 eV). The comparison allows estimating that the maximum systematic error is on the order of 1–2 eV which together with the data in Fig. 7 implies strongly that in the minimum-B ECRIS plasma the ions are hotter by an order of magnitude than previously thought. Furthermore, the result suggests that ion dynamics in the pre-sheath

do not artificially inflate the measured ion temperatures of the minimum-B ECRIS as the plasma potential is in the same order of magnitude, i.e.  $\sim 10$  V, in all aforementioned discharges.

Further assurance of eliminating any possible instrumental effect causing a systematic error in the calculated ion temperatures was sought by measuring the line broadening of a specific emission line of nitrogen utilizing the first and second order diffractions in the monochromator. The 399 nm emission line was chosen as it allows measuring the second order diffraction thanks to its high intensity and wavelength, compatible with the monochromator (second order diffraction at grating position corresponding to 800 nm or less). The instrumental broadening of the second order diffraction is 50 % of the first order broadening as indicated by Eq. 14. Thus, if there was a systematic error affecting the measured line widths, the ion temperatures calculated from different order diffractions would presumably differ from each other. However, the corresponding ion temperatures differ less than 0.6 % from their average, which reasserts the claim that the instrumental effects are well-understood and there are no systematic errors in measuring the linewidths with the described setup.

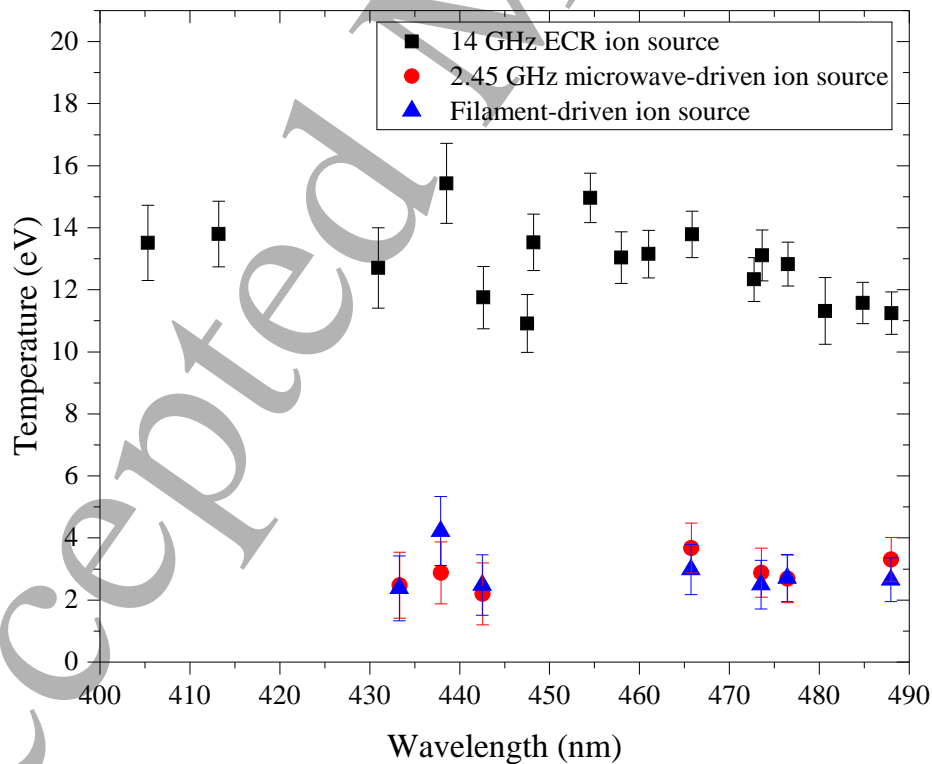


**Figure 8.** The ion temperature of  $\text{Ar}^{1+}$  in the JYFL 14 GHz ECRIS, 2.45 GHz microwave ion source and a filament-driven multicusp ion source determined from emission lines in 400–500 nm wavelength range.

## Spectroscopic study of ion temperature in minimum-B ECRIS plasma

20

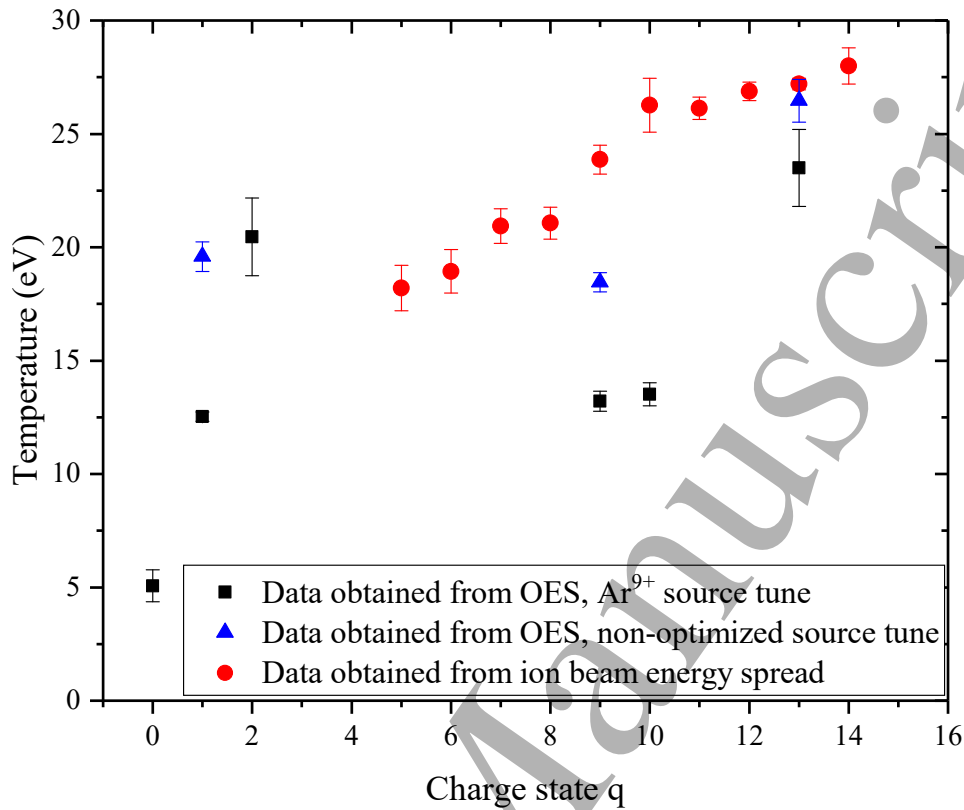


**Figure 9.** The ion temperature as a function of the argon charge state measured from the plasmas with OES and from the beam with the retarding field analyzer. Two sets of data are shown for the charge states accessible with OES - the black squares correspond the ion source tune maximizing the production of  $\text{Ar}^{9+}$  beam current and the blue triangles a non-optimized source tune.

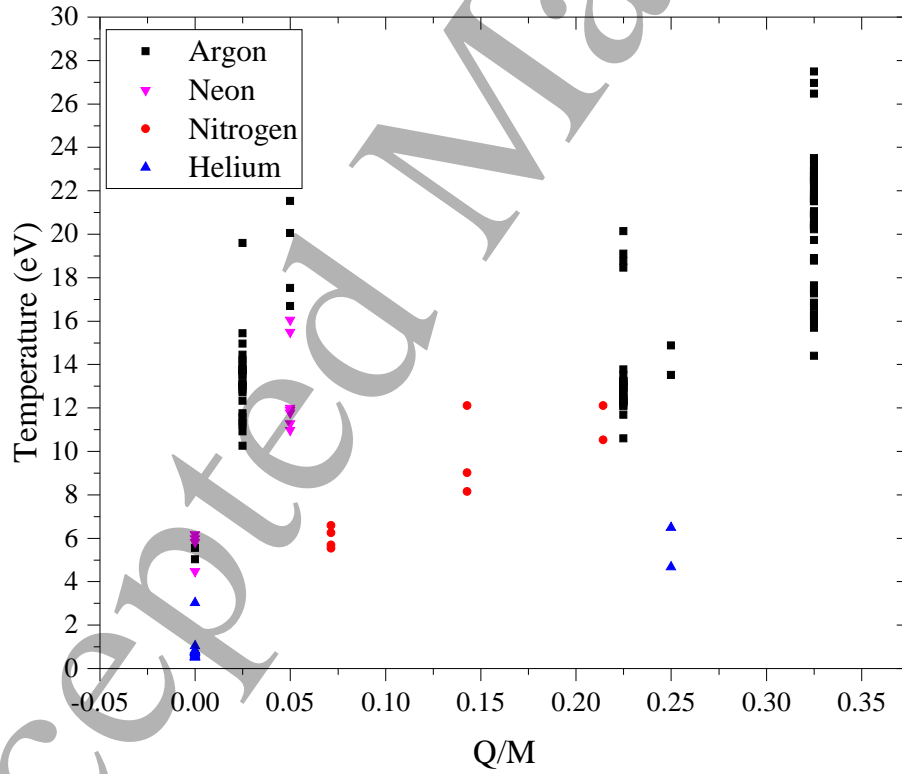
Figure 9 shows the ion temperatures of different charge states of argon measured with the JYFL 14 GHz ECRIS. Three data series are presented; two measured with OES showing the accessible charge states (with detectable transitions in the wavelength range of the spectrometer) and one obtained earlier with the retarding field analyser (previously unpublished). The difference between the OES data series is the tune of the ion source. The first series was obtained when the ion source was tuned for the maximum production of  $\text{Ar}^{9+}$  beam whereas the second one represents a non-optimized source tune at comparable microwave power. The following observations can be made: (i) the ion temperature is not the same for all charge states, (ii) the optical data agrees well with the energy analysis of the extracted beams although the effective ion temperature of the extracted ions, measured from the beam energy spread, is higher than the ion temperature in the plasma (similar to Constance-B [14]), and (iii) optimizing the production of  $\text{Ar}^{9+}$  results in a drop of the ion temperature of charge states  $\text{Ar}^{9+}$  and  $\text{Ar}^{10+}$  (observed consistently throughout the experiments).

Figure 10 shows a collection of ion temperature data measured with different

# Spectroscopic study of ion temperature in minimum-*B* ECRIS plasma

21

elements (argon, neon, nitrogen and helium§) and ion source operational parameters, namely the microwave power, neutral gas pressure and magnetic field strength  $B_{\text{inj}}/B_{\text{ext}}/B_{\text{min}}$  (injection, extraction and minimum) ranging from 100 W,  $1 \cdot 10^{-7}$  mbar and 2.00 T/0.92 T/0.34 T to 650 W,  $1 \cdot 10^{-6}$  mbar and 2.06 T/0.96 T/0.37 T, respectively. The pressure is monitored with a Penning gauge connected to the radial port of the vessel surrounding the plasma chamber i.e. the given range must be considered only as an indicative measure of the true pressure in the plasma chamber. It was observed with all the elements that the ion temperature is higher than previously thought and it tends to increase with increasing charge state (charge to mass -ratio,  $Q/M$ ), which is also contrary to the generally accepted notion of all charge states having equal temperatures Ref. [7]. This tendency, however, is strongly affected by the ion source tune with the high charge state ion temperatures typically being reduced when their extracted currents are optimized.



**Figure 10.** The neutral and ion temperatures of argon, neon, nitrogen (from molecular  $N_2$ ) and helium in ECRIS plasma as a function of charge to mass -ratio ( $Q/M$ ).

§ The emission lines of the hydrogen-like  $He^+$  are degenerate and their fine-structure cannot be resolved with the described spectrometer. The corresponding effect on the measured line broadening is unknown, which implies a higher uncertainty of  $He^+$  ion temperatures in comparison to other ions and neutrals in Fig. 10

*Spectroscopic study of ion temperature in minimum-B ECRIS plasma* 22

Before discussing the implications of the higher-than-expected ion temperatures and possible ion heating mechanisms in ECRIS plasmas we present the temperatures of  $\text{Ar}^{13+}$  as a function of the microwave power (14 GHz) as well as a comparison of  $\text{Ar}^{9+}$  and  $\text{Ar}^{13+}$  temperatures under single (14 GHz) and double frequency (14 and 11.5 GHz) heating modes. The data are shown in Figs. 11 and 12. The figures demonstrate that the high charge state argon temperature first increases rapidly with the microwave power and then saturates or increases very slowly similar to the hot electron temperature and plasma energy content, probed by measuring the plasma diamagnetism [1, 30], and therefore indicating a link between electron heating (formation of the potential dip) and ion temperature as discussed in the following section. A small difference between the ion temperatures in single and double frequency heating modes was observed for  $\text{Ar}^{9+}$  with the average temperatures of  $12.3 \pm 0.4 \text{ eV}$  and  $13.1 \pm 0.3 \text{ eV}$  averaged across the range of 320–420 W total power whereas the ion temperatures of  $\text{Ar}^{13+}$  at 520–620 W total power were essentially the same for both plasma heating modes. The data points shown in Fig. 11 for 500–600 W match to those show in Fig. 12 within the error bars. It is worth noting that the majority of  $\text{Ar}^{13+}$  ion temperatures in Fig. 12 measured in single frequency heating mode at powers exceeding 550 W correspond to a discharge regime where kinetic instabilities were detected. The implications of this observation are discussed in Section 5.



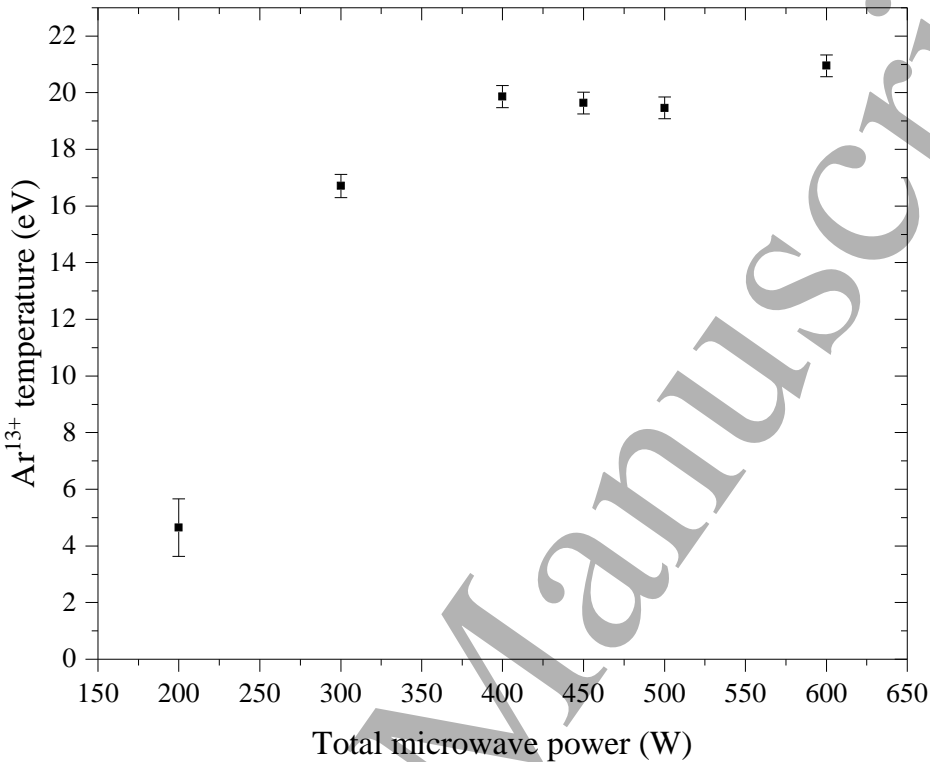


**Figure 11.** The Ar<sup>13+</sup> ion temperature as a function of injected microwave power.

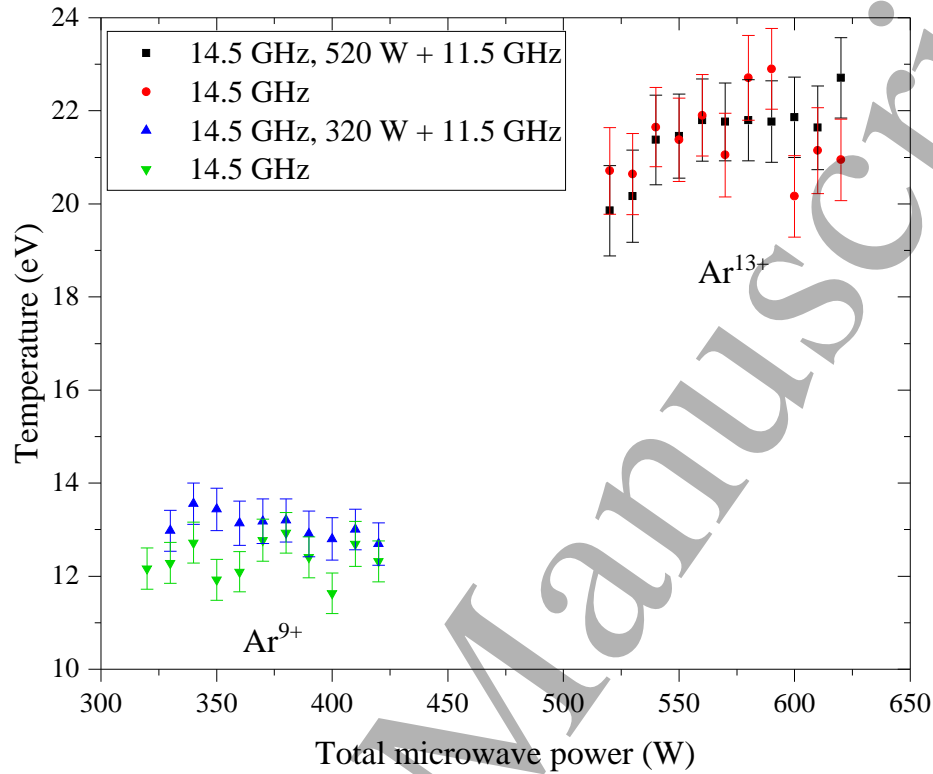


**Figure 12.** The ion temperatures of  $\text{Ar}^{9+}$  and  $\text{Ar}^{13+}$  as a function of total microwave power in single (14 GHz) and double frequency (14 GHz and 11.5 GHz) heating modes.

All ion temperatures derived from the OES results discussed so far were measured from the radial port of the ECRIS. It was confirmed that the results are not affected by geometrical effects (plasma drifts and/or rotation) by comparing ion temperatures measured from the radial and axial viewports yielding the values listed in Table 1 at identical source parameter settings. The ion temperatures measured from different viewports are within the experimental error, which implies that geometrical effects or emission from the plasma chamber wall do not affect the measurement or explain the ion temperature. The intensities of high charge state emission lines detected from the axial viewport observing the peripheral plasma are significantly lower than those detected from the radial port viewing the plasma core, which affects the magnitude of the error bars. The observation matches with the simulated spatial distribution of different charge states [9], i.e. the high charge states presumably populating the plasma core and low charge states found predominantly in the peripheral plasma region.

**Table 1.** Ion temperatures of  $\text{Ar}^+$ ,  $\text{Ar}^{9+}$  and  $\text{Ar}^{13+}$  measured from the radial and axial viewports under similar ion source operational parameters i.e. 500 W microwave power,  $1.5 \cdot 10^{-7}$  mbar pressure and magnetic field  $B_{\text{inj}}/B_{\text{ext}}/B_{\text{min}}$  of 2.02 T/0.93 T/0.35 T.

Charge state ( $q$ )	Temperature from radial viewport	Temperature from axial viewport
1	$16.0 \pm 0.7$ eV	$16.1 \pm 0.7$ eV
9	$18.4 \pm 0.5$ eV	$19 \pm 3$ eV
13	$25 \pm 1$ eV	$22 \pm 2$ eV

## 5. Discussion

The ion temperatures derived from the OES and ion beam energy spread measurements of the JYFL 14 GHz ECRIS are consistent with those obtained earlier with the Constance-B quadrupole machine [15, 14]. Both experiments indicate that the ion temperature in minimum-B ECR devices is significantly higher than previously considered [7]. Although the exact path for the ions to acquire their kinetic energy is unknown, possible ion heating mechanisms can be discussed and assessed based on the experimental data presented above. These include (i) microinstabilities, (ii) conversion of chemical potential to ion kinetic energy (applicable for molecular gas species), (iii) electron-ion collisions (electron drag) combined with long ( $>10$  ms) ion confinement time leading to energy equipartition between the cold electrons and ions, (iv) ion heating through charge exchange collisions and (v) ion heating through electron impact ionization in spatially varying plasma potential (dip). Additionally, the measured ion temperatures allow discussing their implications on the understanding of ECRIS physics.

### 5.1. Ion heating mechanisms in ECRIS plasmas

(i) The higher-than-expected ion temperatures measured for the Constance-B device were attributed to turbulent heating by electron microinstabilities of kinetic origin [14, 31]. Kinetic instabilities are known to give rise to electric fields expelling hot electrons from the minimum-B confinement and have been detected with the JYFL 14 GHz ECRIS [32]. Such instabilities occur when the anisotropy and hot electron fraction of the electron velocity distribution exceed a certain threshold – a process that can be controlled by adjusting the strength of the ECRIS magnetic field ( $B_{\text{min}}/B_{\text{ECR}}$ -ratio) and to some degree the neutral gas pressure and microwave power. Most importantly, the instabilities can be suppressed by applying microwave power at a secondary frequency [33]. Thus, the double-frequency experiment discussed in the previous section serves as a test for the hypothesis of the instability-driven ion heating since periodic instabilities were detected with a scintillator detector measuring bursts of bremsstrahlung caused by high energy electrons escaping the confinement in the single frequency heating mode when the ion source was tuned for the production of  $\text{Ar}^{13+}$  whereas the instabilities were suppressed as the microwave power at the secondary frequency of 11.5 GHz was applied. The ion temperatures being virtually identical in both operation modes indicates that

the kinetic instabilities alone can not explain the anomalous ion temperatures.

(ii) The conversion of chemical potential, namely the molecular binding energy, to ion kinetic energy through dissociation from repulsive molecular states could potentially lead to increased ion temperature as the fragments carry away the typical few eV Franck-Condon energy associated with the process. This should however manifest itself as increased ion temperature in the case of molecular gas species such as nitrogen in comparison to noble gases. Such a trend was not observed in the experiment (see Fig. 10) and, therefore, it is concluded that molecular dissociation does not dictate the ion temperature in ECRIS plasmas.

(iii) If the ions were to gain energy from the cold electron population, they must spend considerable lengths of time confined within the plasma, owing to the low electron-ion momentum transfer rate. Traditionally, the ion confinement times have been considered to be too short, i.e. on the order of a millisecond, for this heating method to be relevant [7, 8]. Experimental methods, however, place the estimate of the cumulative ion confinement time in the tens of milliseconds [34, 35] — a result recently corroborated by experiments made using the JYFL 14 GHz ECRIS [36]. It is argued in Ref. [36], that the confinement times found in the literature are actually measures of the confinement of the escaping ion population. This is because the confinement times are conventionally obtained (see e.g. [8]) from the saturation beam current, which is comprised solely of the unconfined portion of the ion population. The transient method applied in Refs. [34, 35, 36], on the other hand, probes the entire ion population. In response, the cumulative confinement time, measuring the lifetime of a given particle, from the moment it is injected as neutral to the moment it is extracted at the charge state  $q$ , is introduced in [36]. It is this long cumulative confinement time which could allow the ion populations to obtain high temperatures via heating by the electron-drag.

The effect of the electron drag on the ion temperature can be determined from the ion energy balance equation [7]

$$\frac{d\left(\frac{3}{2}n_i^q T_i^q\right)}{dt} = \frac{3}{2}n_e \frac{(T_e - T_i^q)}{\tau_{eq}^{e \rightarrow q}} - \sum_{q'} \frac{3}{2}n_i^q \frac{(T_i^q - T_i^{q'})}{\tau^{q \rightarrow q'}} - \frac{3}{2}n_i^q \frac{T_i^q}{\tau_i^q}, \quad (15)$$

where it is assumed, that the ions of different charge states gain energy in collisions with electrons (first term), transfer it between themselves via ion-ion collisions (second term), and lose it via diffusion or transport processes (third term). The energy transfer between electrons and ions occurs in the timescale  $\tau_{eq}^{e \rightarrow q}$ , which is determined by the electron-ion energy equipartition rate  $\nu_{eq}^{e \rightarrow q}$  according to [7]

$$\frac{1}{\tau_{eq}^{e \rightarrow q}} \sim \nu_{eq}^{e \rightarrow q} \simeq \frac{3.2 \cdot 10^{-9} \ln \Lambda n_i^q q^2}{T_e^{3/2} A} \quad (\text{s}^{-1}, \text{eV}, \text{cm}^{-3}) \quad (16)$$

The ion-ion collision frequency  $\nu_{ii}$  [7] between ions of the same species is used as an approximation of the ion-ion energy equipartition time  $\tau^{q \rightarrow q'}$  such that

$$\frac{1}{\tau^{q \rightarrow q'}} \sim \nu_{ii} \simeq \frac{6.8 \cdot 10^{-8} \ln \Lambda}{(T_i^q)^{3/2}} \frac{q^2}{\sqrt{A_i}} n_e q_{eff} \quad (\text{s}^{-1}, \text{eV}, \text{cm}^{-3}), \quad (17)$$

The ion confinement time  $\tau_i^q$  is assumed to be equal to the ion energy confinement time, and assuming electrostatic confinement of ions within a potential dip in the plasma potential profile, it is given by [6]

$$\tau_i^q = \frac{R\sqrt{\pi}L}{v_T} \exp\left(\frac{|qe\Delta\phi|}{T_i^q}\right), \quad (18)$$

where  $\Delta\phi$  is the depth of the potential dip relative to the peak of the plasma potential,  $v_T = \sqrt{2T_i^q/m}$  the ion thermal velocity,  $R$  the mirror ratio and  $L$  the characteristic length of the plasma.

The ion energy balance equation 15 can — in part — explain the observed  $Q/M$ -dependence of the ion temperatures. The rate of change of the ion temperature depends on the energy exchange rate and ion confinement time as

$$\frac{dT^q}{dt} \propto \nu_{eq}^{e \rightarrow q} - \frac{T^q}{\tau^q} \propto \frac{q^2}{A} - \frac{T^q}{e^{q\Delta\phi/T^q}}. \quad (19)$$

It can be seen that the rate of ion temperature change increases with longer confinement time and higher electron-ion energy equipartition rate. Both of these factors depend on the ion charge state causing the higher charge states to absorb energy at a greater rate. The temperature gain of an ion population ultimately ceases, when the confinement time and energy exchange rates are in equilibrium, i.e.  $dT^q/dt = 0$ .

Equation 15 defines a system of equations for ions of species  $i$  and charge states  $q = 1, 2, \dots, N$ , which absorb energy in collisions with the cold electron population. The hot, ECR-heated electron population accounting for the ionization of high charge state ions in the plasma core does not contribute significantly to the ion temperature in the electron-drag model, due to the inefficiency of the energy transfer at high electron temperatures. This system can be numerically solved in the steady state ( $d/dt = 0$ ) to obtain the ion temperatures. In addition, it is assumed here that the ions only interact with their neighboring charge states, i.e. the sum over  $q'$  in equation 15 is limited to  $q' = (q - 1, q, q + 1)$ . This condition was included based on the spatial charge state distribution as obtained through simulations [9], which show that the different charges dwell in different locations within the plasma volume, with high charge states in the plasma core and lower charges in the peripheral plasma. This causes a source of error, because the ion-ion collision frequency already assumes collisions between all charge states, which is a necessary evil as the ion densities are unknown. Solving the ion temperatures separately for each charge state expands the approach adopted in Ref. [7], where all ions were assumed to have the same temperature, to better reflect the experimental observations.

The numerically calculated ion temperatures are plotted in Fig. 13 as a function of the cold electron temperature assuming a potential dip depth of 1 V (left) and 5 V (right). These potential dip values were chosen to represent a commonly accepted 1 V order-of-magnitude [12] and a value of  $\Delta\phi = kT_i/2$  [5], yielding 5 V based on the experimental  $\sim 10$  eV ion temperature. It can be seen that the ions may acquire rather high temperatures of  $>10$  eV given a cold electron temperature of  $>20$  eV and

a potential dip of a few volts. The ion temperatures are seen to saturate with the (cold) electron temperature, due to the decrease in the effectiveness of the electron-ion heating and the increased ion loss rates as the ions gain energy, which increases their diffusive losses. In the saturation region the numerical solution becomes unstable, which is why the calculations were only performed up to electron temperatures of 20 eV and 30 eV, respectively. The effect of the potential dip depth is evident from the figure; the effectiveness of the electrostatic confinement depends strongly on the value of the potential dip allowing only those ions with sufficient energies to escape, which is reflected in the ion temperature. In other words, as the temperature of a population increases, so does the fraction of ions able to escape. An analysis of the different terms in equation 15 shows, that the high charge states absorb energy from the cold electron population at a higher rate than their energy is depleted via diffusion. This energy is then distributed to the lower charge states – essentially immediately – via ion-ion collisions. It is worth emphasizing that the numerical result in Fig. 13 implies that the ion temperature increases with the charge state, thus matching the experimental observation, with the high charge states being more sensitive to variations of the cold electron temperature above 10 eV.

(iv) Charge exchange, the process where a positively charged ion captures an electron from the outer shell of a neutral atom i.e.  $A^{q+} + B \rightarrow A^{(q-1)+} + B^+$ , can potentially heat the ions in the ECRIS plasma. This is due to the conversion of the (electric) potential energy of the two ions into their kinetic energy as they repel each other after the charge exchange reaction. The maximum kinetic energy acquired by the  $A^{(q-1)+}$  and  $B^+$  ions (the species A and B are the same in the following example) can be calculated by interpreting the charge exchange cross section  $\sigma$  as geometrical area  $\sigma = A = \pi R_0^2$ , where  $R_0$  is the distance between the two particles where the force binding the outer shell electron to the neutral atom equals the attractive force exerted on it by the positive ion. The resulting charge exchange cross section [37] is of the form

$$\sigma_{q,q-1} = \pi a_0^2 q \left( \frac{I_0}{I} \right)^2 Z_{\text{eff}}, \quad (20)$$

where  $a_0$  is the Bohr radius,  $q$  the charge state of the ion,  $I_0$  the ionization potential of hydrogen (13.6 eV),  $I$  the first ionization potential of the neutral atom and  $Z_{\text{eff}}$  the effective atomic number of the ion experienced by the valence electron of the neutral atom ( $Z_{\text{eff}} \neq Z$  due to electron cloud screening effect). The cross sections derived from the above equation are in good agreement with experimental results [38, 39]. The conversion of the potential energy into ion kinetic energy can be estimated by calculating the ion energies acquired as they distance from each other. It is assumed here that the electric field  $E$  experienced by each ion is of the form

$$E = E_0 e^{-\frac{r}{\lambda_D}} = \frac{Q}{4\pi\epsilon_0} \frac{e^{-\frac{r}{\lambda_D}}}{r^2}, \quad (21)$$

where  $E_0$  is the electric field of a point charge  $Q$  ( $Q$  is either  $(q-1)e$  or  $e$  where  $e$  is the elementary charge) and  $\lambda_D$  is the local Debye length of the ECR discharge. As

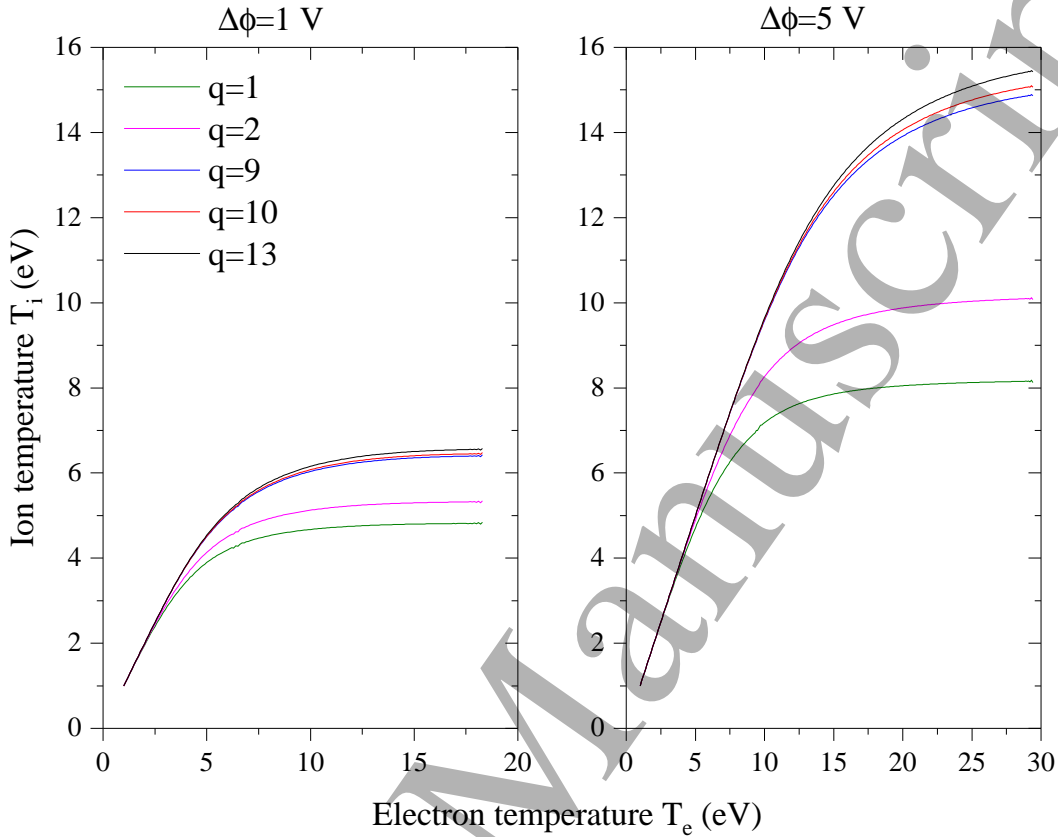


**Figure 13.** Argon ion temperatures predicted by equation 15 assuming ion confinement within a potential dip of  $\Delta\phi = 1$  V (left) and  $\Delta\phi = 5$  V (right). The numerical calculation is performed for a pure argon plasma with  $n_e = 5 \cdot 10^{11} \text{ cm}^{-3}$ ,  $\ln \Lambda = 12$  and  $R = 2$  estimated for the JYFL 14 GHz ECRIS.

an example Table 2 shows numerically integrated energies of  $1+$  and  $(q-1)+$  Ar ions acquired after a charge exchange reaction. It is assumed that the kinetic energy is acquired when the ions move apart from a distance of  $R_0$  to five Debye lengths where the electric field has decreased to less than a percent of the unscreened field of a point charge, and the resulting energy is distributed equally between the ions i.e. both charges are moving apart from each other. The local Debye length of the ECRIS plasma is considered to be determined by the cold,  $\sim 10$  eV electron population having a density on the order of  $10^{11}$ – $10^{12} \text{ cm}^{-3}$ , yielding a value of approximately  $5 \cdot 10^{-5} \text{ m}$ .

The (maximum) kinetic energies listed in Table 2 suggest that charge exchange reactions could contribute significantly to ion heating in ECRIS plasmas as the energy acquired by the receding charges is distributed to an ensemble of ions through ion-ion collisions. However, the volumetric rate of this ion heating process depends strongly on the neutral density. The characteristics of the charge exchange induced ion heating are consistent with four experimental observations: (a) the order of magnitude of the acquired energies matches well with the OES data, (b) most importantly charge

**Table 2.** Charge exchange cross sections and maximum energies of argon ions acquired through Coulomb repulsion in a charge exchange reaction.

Charge state ( $q$ )	Cross section [ $10^{-19}$ m <sup>2</sup> ]	Ion kinetic energy [eV]
2	0.89	8.6
3	1.33	10.5
4	1.78	12.1
5	2.22	13.5
6	2.67	14.8
7	3.11	16
8	3.56	17.1
9	4.00	18.2
10	4.44	19.1
11	4.89	20.1
12	5.33	21
13	5.78	21.8
14	6.22	22.6
15	6.67	23.4
16	7.11	24.2
17	7.56	24.9
18	8.00	25.7

exchange could explain why  $1+$  ions that do not have time to exchange energy with the electron population are measured to be relatively hot ( $\sim 10$  eV in the case of argon), (c) high- $Z$  elements for which the charge exchange cross sections are larger have higher temperatures and (d) high charge states that have larger charge exchange cross sections have higher temperatures.

(v) Yet another process that could contribute to ion heating is ionization in the spatially varying electrostatic potential, i.e. inside the potential dip that is believed to confine the ions electrostatically. This heating mechanism can be best explained considering the following simplified example ignoring energy equipartition through collisions. Let's assume that an ion with a charge state  $q$  has an (initial) energy of  $E_i$  at the bottom of the potential dip. If  $E_i$  is not sufficient to overcome the potential barrier, the ion is confined and as it moves in the potential well its kinetic energy  $E_k$  varies in the range of  $0 \leq E_k \leq E_i = qV_{max}$  where  $V_{max}$  is the potential at the turning point of the ion i.e. the kinetic energy is converted into potential energy and vice versa depending on the local electric potential. If the ion undergoes ionization, potential energy is converted into kinetic energy now varying in the range of  $0 \leq E_k \leq (q+1)V_{max}$ . In other words ionization can gradually heat the ions but does not explain how they eventually can exit the potential dip. Such a process is analogous to the heating of so-called Yushmanov-trapped ions, which are presumably caught between a magnetic mirror peak and the peak of the plasma potential barrier and gaining energy proportional to their charge



state as hypothesized in Ref. [14] to explain the deviation between the ion temperatures obtained through OES and end-loss energy analysis. Although the heating through ionization could explain the ion temperature increasing with the charge state, it fails to account for the anomalous temperature of the 1+ ions as well as the difference between the elements.

The relative importance of each ion heating mechanism cannot be conclusively assessed based on the existing experimental data. However, the electron drag and charge exchange combined with electrostatic ion confinement are the most likely processes to account for the  $\sim 10$  eV ion temperature increasing with the ion charge state. The microwave power dependence of the ion temperature (Fig. 11) implies a connection between the plasma energy content [30], i.e. hot electron density and temperature and the ion temperature, which could be explained by the accumulation of hot electrons [40] affecting the depth of the potential dip. On the other hand the high temperature of the 1+ ions would be best explained by charge exchange reactions. The rate of ion heating through charge exchange reactions would depend on the neutral density and its spatial variation in the ECRIS plasma affecting the equipartition of the energy gained in single charge exchange reaction. Although the experiments have established that the ion temperatures in ECRIS plasmas are higher than expected and helped to identify possible mechanisms accounting for the discrepancy, it can be concluded that further experiments probing the connection between plasma energy content, cumulative ion confinement time and neutral particle density are required to identify the contribution of each process. The data provided here can be used for designing follow-up experiments.

### 5.2. Implications of the measured ion temperatures

The higher-than-expected ion temperature has implications on the quality of the ion beams extracted from ECR ion sources as well as the collisionality of the ions in ECRIS plasma, which affects e.g. the capture of the injected 1+ ion beam in charge breeders. The (theoretical) ratio of the transverse normalized-rms-emittances due to ion temperature and (decrease of the) magnetic field at the extraction can be written as [11, 41]

$$\eta = \frac{\epsilon_{rms,n}^{T_i}}{\epsilon_{rms,n}^B} = \frac{4}{r} \frac{\sqrt{mkT_i}}{Bq}, \quad (22)$$

where  $r$  is the radius of the extraction aperture,  $kT_i$  is the ion temperature,  $m$  is the ion mass,  $q$  is the ion charge and  $B$  is the magnetic field at the extraction. This means that the contribution of the ion temperature on the emittance of the extracted beam could be more than three times higher than previously thought as the ion temperature is higher by an order of magnitude i.e.  $\sim 10$  eV instead of  $\sim 1$  eV. For the JYFL 14 GHz ECRIS the radius of the extraction aperture and magnetic field at the extraction are 4 mm and 0.9 T, respectively. Hence, for 10 eV  $\text{Ar}^{8+}$  ion the above ratio is approximately 0.3 i.e. the contribution of the ion temperature on the transverse emittance could be more

than 20 % instead of the negligible few percent as previously thought. For high charge states that are shown to be even hotter and are extracted near the source axis from an effective radius smaller than the extraction aperture [42, 43], the contribution of the thermal emittance is even larger.

In addition to having an influence on the quality (emittance and longitudinal energy spread) of the extracted beams, the higher-than-expected ion temperature has implications on the modeling of the 1+ ion capture process of charge breeder ion sources and the interpretation of 1+ injection diagnostics. It is generally believed that the capture process in ECRIS charge breeders is a consequence of cumulative small-angle scatterings of the incident 1+ ions in ion-ion collisions [44]. The slowing down coefficient [45] of the 1+ ions reaches its maximum when the longitudinal component of the incident ion velocity equals the average velocity of the plasma ions. Experimental and simulation studies [46, 12] of the 1+ ion capture at different injection energies have lead to the conclusion that the ion temperature in the ECRIS plasma is below 1 eV if the capture process is indeed dominated by cumulative ion-ion collisions. Such a notion contradicts the experimental results presented herein, therefore suggesting that electron impact ionization of the injected 1+ enhancing the Coulomb interactions could instead be the primary capture mechanism. The situation calls for measurements of the ion temperature in charge breeder ECR ion sources.

## Acknowledgments

The authors would like to thank P. Myllyperkiö, T. Suppala, I. Moore, S. Geldhof, M. Liimatainen and the JYFL electrical and mechanical workshop for their help with technical issues and spectrometer calibration. The project has received funding from the European Unions Horizon 2020 research and innovation programme under grant agreement N:o 654002 and the Academy of Finland under the Finnish Centre of Excellence Programme 2012–2017 (Nuclear and Accelerator Based Physics Research at JYFL, Project N:o 213503) and the Academy of Finland Project funding (N:o 315855).

## References

- [1] C. Barué, M. Lamoureux, P. Briand, A. Girard and G. Melin, *Journal of Applied Physics* **76**, p. 2662-2670 (1994).
- [2] V. P. Pastukhov, *Review of Plasma Physics*, **13**, p. 203-259 (1987).
- [3] R. Geller, *Electron Cyclotron Resonance Ion Sources and ECR Plasmas* (Institute of Physics, Philadelphia, PA, 1996).
- [4] G. D. Shirkov, *Plasma Sources Science Technology*, **2**, p. 250-257 (1993).
- [5] D. Mascali, L. Neri, L. Celona, G. Castro, G. Torrissi, S. Gammino, G. Sorbello, and G. Ciavola, *Review of Scientific Instruments* **85**, p. 02A511 (2014).
- [6] T. Rognlien and T. Cutler, *Nucl. Fusion* **20**, (1980), p. 1003.
- [7] G. Melin and A. G. Drentje and A. Girard and D. Hitz, *Journal de Physique Colloques* **86**, p. 4772-4779 (1999).
- [8] G. Douysset, H. Khodja, A. Girard and J. P. Briand, *Phys. Rev. E*, **61**, 3, (2000), p. 3015.

- [9] V. Mironov, S. Bogomolov, A. Bondarchenko, A. Efremov and V. Loginov, Phys. Rev. ST Accel. Beams **18**, p. 123401 (2015).
- [10] A. Girard, D. Hitz, G. Melin, and K. Serebrennikov, Rev. Sci. Instrum. **75**, 1381 (2004).
- [11] V. Toivanen, T. Kalvas, H. Koivisto, J. Komppula and O. Tarvainen, J. Instrum. **8** (2013) P05003.
- [12] A. Galatà, D. Mascali and L. Neri and L. Celona, Plasma Sources Science and Technology, **25** (2016) P045007.
- [13] O. Tarvainen, P. Suominen, T. Ropponen, H. Koivisto, R.C. Vondrasek and R.H. Scott, Proc. 16th International Workshop on ECRIS, Berkeley, (2004), p.61.
- [14] C. Petty, D. Goodman, D. Smith, D. Smatlak, Journal de Physique Colloques **50**, p. C1-783-C1-789 (1989).
- [15] C. C. Petty and D. L. Goodman and D. L. Smatlak and D. K. Smith, Physics of Fluids B: Plasma Physics **3**, p. 705-714 (1991).
- [16] S. D. Baalrud, C. C. Hegna and J. D. Callen, Phys. Rev. Lett. **103**, 205002 (2009).
- [17] R. Kronholm and T. Kalvas and H. Koivisto and O. Tarvainen, Review of Scientific Instruments **89**, p. 043506 (2018).
- [18] H. Koivisto, P. Heikkinen, V. Hänninen, A. Lassila, H. Leinonen, V. Nieminen, J. Pakarinen, K. Ranttila, J. Ärje and E. Liukkonen, Nucl. Instrum. Meth. B **174**, p. 379 - 384 (2001).
- [19] W. L. Wiese, M. W. Smith and B. M. Miles, NSRDS-NBS, Washington, D.C.: US Department of Commerce, National Bureau of Standards, —c 1969.)
- [20] G.W.F. Drake, Atomic, Molecular, Optical Physics Handbook, Chaps. 19 and 57, (AIP, Woodbury, NY, 1996).
- [21] A. W. Ali, H. R. Griem, Phys. Rev., **140** (1965) p. A1044–A1049.
- [22] M. A. Gigosos, Journal of Physics D: Applied Physics, **47**, p. 343001 (2014).
- [23] N. Konjević and W.L. Wiese, Journal of Physical and Chemical Reference Data, **19**, p. 1307-1385 (1990).
- [24] J. Muñoz and M.S. Dimitrijevi and C. Yubero and M.D. Calzada, Spectrochimica Acta Part B: Atomic Spectroscopy **64**, p. 167 - 172 (2009).
- [25] A. S. Taylor, A. R. Hyde and O. V. Batishchev, American Journal of Physics **85**, 565 (2017).
- [26] L. Yang, X. Tan, X. Wan, L. Chen, D. Jin, M. Qian and G. Li, Journal of Applied Physics **115**, 163106 (2014).
- [27] O. Tarvainen, P. Suominen and H. Koivisto, Rev. Sci. Instrum. **75**, (2004), p. 3138.
- [28] J. Komppula, O. Tarvainen, T. Kalvas, H. Koivisto, R. Kronholm, J. Laulainen and P. Myllyperkiö J. Phys. D **48**, 365201 (2015).
- [29] J. Laulainen, S. Aleiferis, T. Kalvas, H. Koivisto, R. Kronholm, and O. Tarvainen, Phys. Plasmas **24**, 103502 (2017).
- [30] J. Noland, O. Tarvainen, J. Benitez, D. Leitner, C. Lyneis and J. Verboncoeur, Plasma Sources Sci. Technol. **20** 035022 (2011).
- [31] R. C. Garner, a M. E. Mauel, b S. A. Hokin, R. S. Post, and D. L. Smatlak, Phys. Rev. Lett. **59**, 1821, (1987).
- [32] O. Tarvainen, I. Izotov, D. Mansfeld, V. Skalyga, S. Golubev, T. Kalvas, H. Koivisto, J. Komppula, R. Kronholm, J. Laulainen and V. Toivanen, 2014 Plasma Sources Sci. Technol. **23** 025020.
- [33] V. Skalyga, I. Izotov, T. Kalvas, H. Koivisto, J. Komppula, R. Kronholm, J. Laulainen, D. Mansfeld, and O. Tarvainen, Phys. Plasmas **22**, 083509 (2015).
- [34] D. Neben, J. Fogleman, D. Leitner, G. Machicoane, G. Parsey, A. Pham, S. Renteria, J. Stetson, L. Tobos, and J. Verboncoeur, Proceedings of ECRIS2016, Busan, Korea, p. 128, (2016)
- [35] D. Neben, G. Machicoane, G. Parsey, A. Pham, J. Stetson, and J. Verboncoeur, Proceedings of LINAC2016, East Lansing, MI, USA, 4B, p. 475, (2016)
- [36] M. Marttinen, *Transient sputtering method for estimating ion confinement times in ECRIS plasma*, Master's thesis, University of Jyväskylä, (2018), full-text available at <https://jyx.jyu.fi/handle/123456789/59650> (unpublished).

**Table A1.** List of optical transitions of helium used for determining the ion (neutral) temperatures in the plasma of the JYFL 14 GHz ECRIS.

Ion species ( $q$ )	Wavelength [nm]	Upper state	Lower state
He <sup>0+</sup>	414.376	1s6d <sup>1</sup> D <sub>2</sub>	1s2p <sup>1</sup> P <sub>1</sub> <sup>o</sup>
He <sup>0+</sup>	438.793	1s5d <sup>1</sup> D <sub>2</sub>	1s2p <sup>1</sup> P <sub>1</sub> <sup>o</sup>
He <sup>0+</sup>	443.755	1s5s <sup>1</sup> S <sub>0</sub>	1s2p <sup>1</sup> P <sub>1</sub> <sup>o</sup>
He <sup>0+</sup>	492.193	1s4d <sup>1</sup> D <sub>2</sub>	1s2p <sup>1</sup> P <sub>1</sub> <sup>o</sup>
He <sup>0+</sup>	501.568	1s3p <sup>1</sup> P <sub>1</sub> <sup>o</sup>	1s2s <sup>1</sup> S <sub>0</sub>
He <sup>0+</sup>	504.774	1s4s <sup>1</sup> S <sub>0</sub>	1s2p <sup>1</sup> P <sub>1</sub> <sup>o</sup>
He <sup>0+</sup>	587.597	1s3d <sup>3</sup> D <sub>1</sub>	1s2p <sup>3</sup> P <sub>0</sub> <sup>o</sup>
He <sup>0+</sup>	667.815	1s3d <sup>1</sup> D <sub>2</sub>	1s2p <sup>1</sup> P <sub>1</sub> <sup>o</sup>
He <sup>1+</sup>	468.570	4f <sup>2</sup> F <sub>5/2</sub> <sup>o</sup>	3d <sup>2</sup> D <sub>3/2</sub>
He <sup>1+</sup>	656.014	6f <sup>2</sup> F <sub>7/2</sub> <sup>o</sup>	4d <sup>2</sup> D <sub>5/2</sub>

- [37] H.Knudsen, H.K.Haugen and P.Hvelplund, Physical Review A, **23**, 2, 597-610, (1981).
- [38] E. Salzborn, IEEE Transactions on Nuclear Science, NS-23 p. 947-958, (1976).
- [39] T. Kusakabe, T. Horiuchi, N. Nagai, H. Hanaki, I. Konomi and M. Sakisaka, Journal of Physics B: Atomic and Molecular Physics, 19 p. 2165-2174, (1986).
- [40] T. Ropponen, O. Tarvainen, I. Izotov, J. Noland, V. Toivanen, G. Machicoane, D. Leitner, H. Koivisto, T. Kalvas, P. Peura, P. Jones, V. Skalyga and V. Zorin, Plasma Sources Sci. Technol. 20 055007, (2011).
- [41] T. Kalvas, "Development and use of computational tools for modelling negative hydrogen ion source extraction systems", Department of Physics, University of Jyväskylä, Research Report No. 10/2013.
- [42] D. Wutte, M. A. Leitner and C. M. Lyneis, Phys. Scripta T92 (2001) 247249.
- [43] L. Panitzsch, T. Peleikis, S. Böttcher, M. Stalder, R. F. Wimmer-Schweingruber, Rev. Sci. Instrum. 84 (2013) 013303.
- [44] R. Geller, T. Lamy and P. Sortais, 2006 Rev. Sci. Instrum. 77 03B107.
- [45] J. L. Delcroix and A. Bers 1994 Physique des Plasmas 2 (Paris: CNRS) p 357.
- [46] O. Tarvainen, T. Lamy, J. Angot, T. Thuillier, P. Delahaye, L. Maunoury, J. Choinski, L. Standlyo, A. Galatà, G. Patti and H. Koivisto, Plasma Sources Sci. Technol. 24 (2015) 035014.
- [47] [https://physics.nist.gov/PhysRefData/ASD/lines/\\_form.html](https://physics.nist.gov/PhysRefData/ASD/lines/_form.html)

## Appendix

The optical transitions [47] used in this work for determining the Doppler broadening are listed in Tables A1–A4.

**Table A2.** List of optical transitions of nitrogen used for determining the ion temperatures in the plasma of the JYFL 14 GHz ECRIS.

Ion species ( $q$ )	Wavelength [nm]	Upper state	Lower state
N <sup>1+</sup>	399.500	$2s^2p3p\ ^1D_2$	$2s^22p3s\ ^1P_1^o$
N <sup>1+</sup>	463.054	$2s^22p3p\ ^3P_2$	$2s^22p3s\ ^3P_2^o$
N <sup>1+</sup>	566.663	$2s^22p3p\ ^3D_2$	$2s^22p3s\ ^3P_1^o$
N <sup>1+</sup>	571.077	$2s^22p3p\ ^3D_2$	$2s^22p3s\ ^3P_2^o$
N <sup>2+</sup>	336.736	$2s2p(^3P^o)3p\ ^4P_{5/2}$	$2s2p(^3P^o)3s\ ^4P_{5/2}^o$
N <sup>2+</sup>	409.736	$2s^23p\ ^2P_{3/2}^o$	$2s^23s\ ^2S_{1/2}$
N <sup>2+</sup>	453.086	$2s2p(^3P^o)3p\ ^4D_{1/2}$	$2s2p(^3P^o)3s\ ^4P_{3/2}^o$
N <sup>3+</sup>	347.872	$1s^22s3p\ ^3P_2^o$	$1s^22s3s\ ^3S_1$
N <sup>3+</sup>	348.300	$1s^22s3p\ ^3P_1^o$	$1s^22s3s\ ^3S_1$

**Table A3.** List of optical transitions of neon used for determining the ion (neutral) temperatures in the plasma of the JYFL 14 GHz ECRIS.

Ion species ( $q$ )	Wavelength [nm]	Upper state	Lower state
Ne <sup>0+</sup>	534.109	$2s^22p^5(^2P_{3/2}^o)4d\ ^2[1/2]_1^o$	$2s^22p^5(^2P_{3/2}^o)3p\ ^2[1/2]_1$
Ne <sup>0+</sup>	607.434	$2s^22p^5(^2P_{3/2}^o)3p\ ^2[1/2]_0$	$2s^22p^5(^2P_{3/2}^o)3s\ ^2[3/2]_1^o$
Ne <sup>0+</sup>	609.616	$2s^22p^5(^2P_{1/2}^o)3p\ ^2[3/2]_2$	$2s^22p^5(^2P_{3/2}^o)3s\ ^2[3/2]_1^o$
Ne <sup>1+</sup>	331.972	$2s^22p^4(^1D)3p\ ^2P_{1/2}^o$	$2s^22p^4(^1D)3s\ ^2D_{3/2}$
Ne <sup>1+</sup>	332.374	$2s^22p^4(^3P)3p\ ^2P_{3/2}^o$	$2s^22p^4(^3P)3s\ ^2P_{3/2}$
Ne <sup>1+</sup>	334.440	$2s^22p^4(^3P)3p\ ^4D_{1/2}^o$	$2s^22p^4(^3P)3s\ ^4P_{1/2}$
Ne <sup>1+</sup>	334.545	$2s^22p^4(^1D)3p\ ^2P_{3/2}^o$	$2s^22p^4(^1D)3s\ ^2D_{5/2}$
Ne <sup>1+</sup>	337.822	$2s^22p^4(^3P)3p\ ^2P_{1/2}^o$	$2s^22p^4(^3P)3s\ ^2P_{1/2}$
Ne <sup>1+</sup>	347.952	$2s^22p^4(^1S)3p\ ^2P_{1/2}^o$	$2s^22p^4(^1S)3s\ ^2S_{1/2}$
Ne <sup>1+</sup>	356.850	$2s^22p^4(^1D)3p\ ^2F_{7/2}^o$	$2s^22p^4(^1D)3s\ ^2D_{5/2}$
Ne <sup>1+</sup>	369.421	$2s^22p^4(^3P)3p\ ^4P_{5/2}^o$	$2s^22p^4(^3P)3s\ ^4P_{5/2}$
Ne <sup>1+</sup>	375.378	$2s^22p^4(^3P)3d\ ^4F_{5/2}$	$2s^22p^4(^3P)3p\ ^2P_{3/2}^o$

**Table A4.** List of optical transitions of argon used for determining the ion (neutral) temperatures in the plasma of the JYFL 14 GHz ECRIS.

Ion species ( $q$ )	Wavelength [nm]	Upper state	Lower state
Ar <sup>0+</sup>	459.610	$3s^23p^5(^2P_{3/2}^o)5p\ ^2[3/2]_1$	$3s^23p^5(^2P_{1/2}^o)4s\ ^2[1/2]_1^o$
Ar <sup>0+</sup>	750.387	$3s^23p^5(^2P_{1/2}^o)4p\ ^2[1/2]_0$	$3s^23p^5(^2P_{1/2}^o)4s\ ^2[1/2]_1^o$
Ar <sup>1+</sup>	397.935	$3s^23p^4(^3P)4d\ ^4P_{1/2}$	$3s^23p^4(^3P)4p\ ^4S_{3/2}^o$
Ar <sup>1+</sup>	405.292	$3s^23p^4(^1S)4p\ ^2P_{3/2}^o$	$3s^23p^4(^1S)4s\ ^2S_{1/2}$
Ar <sup>1+</sup>	413.172	$3s^23p^4(^1D)4p\ ^2P_{1/2}^o$	$3s^23p^4(^1D)4s\ ^2D_{3/2}$
Ar <sup>1+</sup>	427.753	$3s^23p^4(^1D)4p\ ^2P_{3/2}^o$	$3s^23p^4(^1D)4s\ ^2D_{5/2}$
Ar <sup>1+</sup>	430.924	$3s^23p^4(^3P)5p\ ^2P_{3/2}^o$	$3s^23p^4(^1S)4s\ ^2S_{1/2}$
Ar <sup>1+</sup>	438.506	$3s^23p^4(^3P)5p\ ^4D_{3/2}^o$	$3s^23p^4(^1S)4s\ ^2S_{1/2}$
Ar <sup>1+</sup>	442.600	$3s^23p^4(^3P)4p\ ^4D_{5/2}^o$	$3s^23p^4(^3P)4s\ ^4P_{3/2}$
Ar <sup>1+</sup>	447.476	$3s^23p^4(^1D)4p\ ^2P_{1/2}^o$	$3s^23p^4(^3P)3d\ ^2D_{3/2}$
Ar <sup>1+</sup>	448.181	$3s^23p^4(^1D)4p\ ^2D_{5/2}^o$	$3s^23p^4(^3P)3d\ ^2D_{5/2}$
Ar <sup>1+</sup>	454.505	$3s^23p^4(^3P)4p\ ^2P_{3/2}^o$	$3s^23p^4(^3P)4s\ ^2P_{3/2}$
Ar <sup>1+</sup>	457.935	$3s^23p^4(^3P)4p\ ^2S_{1/2}^o$	$3s^23p^4(^3P)4s\ ^2P_{1/2}$
Ar <sup>1+</sup>	460.957	$3s^23p^4(^1D)4p\ ^2F_{7/2}^o$	$3s^23p^4(^1D)4s\ ^2D_{5/2}$
Ar <sup>1+</sup>	465.790	$3s^23p^4(^3P)4p\ ^2P_{1/2}^o$	$3s^23p^4(^3P)4s\ ^2P_{3/2}$
Ar <sup>1+</sup>	472.687	$3s^23p^4(^3P)4p\ ^2D_{3/2}^o$	$3s^23p^4(^3P)4s\ ^2P_{3/2}$
Ar <sup>1+</sup>	473.591	$3s^23p^4(^3P)4p\ ^4P_{3/2}^o$	$3s^23p^4(^3P)4s\ ^4P_{5/2}$
Ar <sup>1+</sup>	476.486	$3s^23p^4(^3P)4p\ ^2P_{3/2}^o$	$3s^23p^4(^3P)4s\ ^2P_{1/2}$
Ar <sup>1+</sup>	480.602	$3s^23p^4(^3P)4p\ ^4P_{5/2}^o$	$3s^23p^4(^3P)4s\ ^4P_{5/2}$
Ar <sup>1+</sup>	484.781	$3s^23p^4(^3P)4p\ ^4P_{1/2}^o$	$3s^23p^4(^3P)4s\ ^4P_{3/2}$
Ar <sup>1+</sup>	487.986	$3s^23p^4(^3P)4p\ ^2D_{5/2}^o$	$3s^23p^4(^3P)4s\ ^2P_{3/2}$
Ar <sup>1+</sup>	496.508	$3s^23p^4(^3P)4p\ ^2D_{3/2}^o$	$3s^23p^4(^3P)4s\ ^2P_{1/2}$
Ar <sup>1+</sup>	514.178	$3s^23p^4(^1D)4p\ ^2F_{7/2}^o$	$3s^23p^4(^3P)3d\ ^2D_{5/2}$
Ar <sup>1+</sup>	514.531	$3s^23p^4(^3P)4p\ ^4D_{5/2}^o$	$3s^23p^4(^3P)4s\ ^2P_{3/2}$
Ar <sup>1+</sup>	611.492	$3s^23p^4(^1D)4p\ ^2F_{7/2}^o$	$3s^23p^4(^1D)3d\ ^2G_{9/2}$
Ar <sup>2+</sup>	333.617	$3s^23p^3(^2D^*)4p\ ^3F_4$	$3s^23p^3(^2D^o)4s\ ^3D_3^o$
Ar <sup>2+</sup>	334.476	$3s^23p^3(^2D^*)4p\ ^3F_3$	$3s^23p^3(^2D^o)4s\ ^3D_2^o$
Ar <sup>2+</sup>	348.050	$3s^23p^3(^2D^*)4p\ ^3D_3$	$3s^23p^3(^2D^o)4s\ ^3D_3^o$
Ar <sup>2+</sup>	351.115	$3s^23p^3(^4S^*)4p\ ^3P_2$	$3s^23p^3(^4S^o)4s\ ^3S_1^o$
Ar <sup>9+</sup>	553.327	$2s^22p^5\ ^2P_{1/2}^o$	$2s^22p^5\ ^2P_{3/2}^o$
Ar <sup>10+</sup>	691.688	$2s^22p^4\ ^3P_1$	$2s^22p^4\ ^3P_2$
Ar <sup>13+</sup>	441.256	$2s^22p\ ^2P_{3/2}^o$	$2s^22p\ ^2P_{1/2}^o$